Department of Micro- and Nanosciences

Synchrotron radiation x-ray topography of crystallographic defects in GaN

Sakari Sintonen

Aalto University

DOCTORAL DISSERTATIONS

Aalto University publication series
DOCTORAL DISSERTATIONS 187/2014

Synchrotron radiation x-ray topography of crystallographic defects in GaN

Sakari Sintonen

A doctoral dissertation completed for the degree of Doctor of Science (Technology) to be defended, with the permission of the Aalto University School of Electrical Engineering, at a public examination held at the large seminar room in Micronova on 12th of December 2014 at 12.

Aalto University
School of Electrical Engineering
Department of Micro- and nanosciences
Nanotechnology

Supervising professor
Prof. Harri Lipsanen

Thesis advisor
Dr. Sami Suihkonen

Preliminary examiners
Prof. Michael Dudley, Stony Brook University, USA

Prof. dr hab. Zbigniew R. Zytkiewicz, Institute of Physics, Polish Academy of Sciences, Poland

Opponent
Dr. Michał Boćkowski, Institute of High Pressure Physics, Polish Academy of Sciences, Poland

Aalto University publication series
DOCTORAL DISSERTATIONS 187/2014

ISBN 978-952-60-5969-3 (printed)
ISBN 978-952-60-5970-9 (pdf)
ISSN-L 1799-4934
ISSN 1799-4934 (printed)
ISSN 1799-4942 (pdf)
http://urn.fi/URN:ISBN:978-952-60-5970-9

Unigrafia Oy
Helsinki 2014

Finland

441 697
Printed matter

Aalto University

Abstract

Aalto University, P.O. Box 11000, FI-00076 Aalto www.aalto.fi

Author
Sakari Sintonen

Name of the doctoral dissertation
Synchrotron radiation x-ray topography of crystallographic defects in GaN

Publisher School of Electrical Engineering

Unit Department of Micro- and Nanosciences

Series Aalto University publication series DOCTORAL DISSERTATIONS 187/2014

Field of research Nanotechnology

Manuscript submitted 15 August 2014 **Date of the defence** 12 December 2014

Permission to publish granted (date) 22 October 2014 **Language** English

☐ **Monograph** ☒ **Article dissertation (summary + original articles)**

Abstract

In this thesis, the crystal structures of bulk, homoepitaxial and heteroepitaxial GaN were characterized by synchrotron radiation x-ray topography (SR-XRT), x-ray diffraction (XRD) and defect selective etching (DSE).

The SR-XRT image contrast of threading screw dislocations and threading mixed dislocations in GaN were determined. The images caused by the strain fields of threading screw dislocations and threading screw dislocation clusters were simulated, and the simulated and experimental topograph images of low defect density ammonothermal GaN were in excellent agreement. Topograph images corresponding to strain fields of large dislocations with Burgers vector magnitudes equal to multiples of the elemental screw dislocation Burgers vector were observed. DSE experiments were performed to determine whether these large defect images originate from single dislocation strain fields, i.e. super screw dislocations or micropipes, or from combined strain fields of several elemental dislocations in close proximity. DSE images revealed that all observations but one were caused by groups of adjacent elemental threading dislocations.

The determined topograph image contrasts of threading mixed and threading screw dislocations were utilized in large area studies of bulk GaN grown by the ammonothermal method. In one of the studies, threading mixed dislocations were observed to form arrays consisting of mixed dislocations with identical Burgers vectors. The minute lattice tilt and twist caused by the dislocation arrays were calculated based on dislocation spacing and confirmed with high resolution XRD measurements. SR-XRT analysis of grain boundaries and basal plane dislocations in ammonothermal GaN were also discussed.

The structural quality of homoepitaxial GaN and heteroepitaxial GaN on patterned substrates was characterized by SR-XRT and XRD. The GaN layers were grown by metallo-organic vapour phase epitaxy (MOVPE) on ammonothermal GaN substrates, patterned sapphire substrates and substrates consisting of patterned MOVPE grown GaN layers on sapphire.

SR-XRT is a technique especially suited for imaging the defect structure of materials with low crystalline defect density, whereas XRD is applicable to characterization of materials with higher defect density as well. SR-XRT measurements enabled imaging of individual dislocations and identification of different dislocation types.

Keywords GaN, dislocations, topography, x-ray diffraction

ISBN (printed) 978-952-60-5969-3 **ISBN (pdf)** 978-952-60-5970-9

ISSN-L 1799-4934 **ISSN (printed)** 1799-4934 **ISSN (pdf)** 1799-4942

Location of publisher Helsinki **Location of printing** Helsinki **Year** 2014

Pages 123 **urn** http://urn.fi/URN:ISBN:978-952-60-5970-9

Aalto-yliopisto

Tiivistelmä

Aalto-yliopisto, PL 11000, 00076 Aalto www.aalto.fi

Tekijä
Sakari Sintonen

Väitöskirjan nimi
GaN:in kidevirheiden synkrotronisäteilyröntgentopografia

Julkaisija Sähkötekniikan korkeakoulu

Yksikkö Mikro- ja nanotekniikan laitos

Sarja Aalto University publication series DOCTORAL DISSERTATIONS 187/2014

Tutkimusala Nanoteknologia

Käsikirjoituksen pvm 15.08.2014 **Väitöspäivä** 12.12.2014

Julkaisuluvan myöntämispäivä 22.10.2014 **Kieli** Englanti

☐ **Monografia** ☒ **Yhdistelmäväitöskirja (yhteenveto-osa + erillisartikkelit)**

Tiivistelmä

Tässä työssä tutkittiin galliumnitridi (GaN) -substraattien, sekä hetero- että homoepitaktisten GaN-kerrosten kiderakenteita synkrotronisäteilyröntgentopografian (SR-XRT), röntgendiffraktion (XRD) ja selektiivisen kidevirhesyövytyksen (DSE) avulla.

Työssä määritettiin ruuvi- ja sekadislokaatioiden topografiakuviin aiheuttamat kontrastimuutokset. Ruuvidislokaatioiden ja ruuvidislokaatiokertymien jännityskenttien vaikutus topografiakuviin määritettiin simuloimalla, ja simuloidut sekä kokeelliset ammonotermisestä GaN-alustasta tallennetut kuvat vastasivat toisiaan erinomaisesti. Tutkimuksessa havaittiin myös topografiakuvia jännityskentistä, jotka vastasivat suuria dislokaatioita, joiden Burgersin vektorit ovat alkeisruuvidislokaation Burgersin vektorin monikertoja. Kyseiset topografiakuvat voivat olla seurausta joko yksittäisistä suurista dislokaatioista, eli superruuvidislokaatioista tai mikroputkista, tai lähekkäin olevien alkeisruuvidislokaatioiden kokoelmasta. DSE-kokeiden avulla havaittiin, että kaikissa, paitsi yhdessä tapauksessa, kyseessä oli useamman dislokaation yhteenlasketun jännityskentän aiheuttamasta topografiakuvasta.

Seka- ja ruuvidislokaatioiden määritettyjä topografiaulkoasuja hyödynnettiin ammonotermisesti kasvatettujen kiteiden laajan alueen kidevirheanalyysissä. Havaittiin, että yhdessä näytteessä sekadislokaatiot muodostivat identtisten Burgersin vektorien dislokaatiojonoja. Kidevirhejonojen aiheuttamat pienet hilakallistukset ja hilapyöritykset laskettiin dislokaatioiden etäisyyksien avulla, ja tulokset todennettiin hyödyntäen korkean resoluution XRD-mittauksia. Työssä analysoitiin myös SR-XRT mittauksien avulla raerajoja ja pohjatason kidevirheitä.

Homoepitaktisten ja heteroepitaktisten GaN-kerrosten kidelaatua tutkittiin SR-XRT:n ja XRD:n avulla. GaN-kerrokset valmistettiin metallo-organic vapour phase epitaxy (MOVPE) -menetelmää käyttäen ammonotermisten GaN-alustojen, kuvioitujen safiirialustojen ja kuvioitujen GaN/safiiri-alustojen päälle. GaN/safiirialustat valmistettiin kuvioimalla safiirin päälle kasvatettuja MOVPE GaN-kerroksia.

SR-XRT on erityisen sopiva menetelmä matalan kidevirhetiheyden materiaalin tutkimiseen. XRD puolestaan soveltuu hyvin myös korkeamman kidevirhetiheyden materiaalien karakterisointiin. SR-XRT mittaukset mahdollistivat yksittäisten dislokaatioiden kuvantamisen sekä dislokaatiotyyppien määrittämisen.

Avainsanat GaN, dislokaatiot, topografia, röntgendiffraktio

ISBN (painettu) 978-952-60-5969-3 **ISBN (pdf)** 978-952-60-5970-9

ISSN-L 1799-4934 **ISSN (painettu)** 1799-4934 **ISSN (pdf)** 1799-4942

Julkaisupaikka Helsinki **Painopaikka** Helsinki **Vuosi** 2014

Sivumäärä 123 **urn** http://urn.fi/URN:ISBN:978-952-60-5970-9

Preface

The research presented in this thesis was carried out at the Department of Micro- and Nanosciences at Aalto University School of Electrical Engineering, former Helsinki University of Technology, during the years 2009-2014.

I am very grateful to Professor Harri Lipsanen for supervising this thesis, and I wish to express my gratitude for giving me the opportunity to conduct research at the Department of Micro- and Nanosciences. I also wish to thank Professor Markku Sopanen for guidance and help in carrying out the work presented in this thesis.

This thesis was excellently instructed by Dr. Sami Suihkonen, and I am immensely grateful for his tireless and insightful input as well as his exceptional perspective on all things scientific. I especially thank Professor Turkka Tuomi for introducing me to and educating me in the field of synchrotron radiation topography, for his invaluable help in writing articles and for all our informal discussions. Thank you co-authors, co-workers and friends Olli Svensk, Dr. Pekka Törmä, Lauri Riuttanen, Perttu Sippola, Henri Jussila, Pasi Kostamo, Dr. Aapo Lankinen, Professor Filip Tuomisto, Professor Seppo Honkanen, Dr. Muhammad Ali, Dr. Mariusz Rudziński, Dr. Andreas Danilewsky, Dr. Elke Meissner, Michael Knetzger, Dr. Romuald Stankiewicz, Dr. Edward Letts, Dr. Sierra Hoff, Dr. Tadao Hashimoto, Dr. Carsten Paulmann, Dr. Marcin Zajac, Dr. Maxim Odnoblyudov and Dr. Vladislav Bougrov.

The thesis was financially supported by the Graduate School in Electronics, Telecommunication and Automation (GETA), the graduate school in Modern Optics and Physics (MOP), Svenska Kulturfonden, Emil Aaltonen foundation, Magnus Ehrnrooth foundation, Ulla Tuominen foundation and Walter Ahlström foundation. I heartily acknowledge these instances and foundations for their ample generosity.

I wish to extend my warmest gratitude and sincere appreciation to my family for the support and encouragement I have received during my studies, and to

Erika for love and last-minute thrust.

Helsinki, 5 November 2014,

Sakari Sintonen

Contents

List of Publications

This thesis consists of an overview and of the following publications which are referred to in the text by their Roman numerals.

I S. Sintonen, M. Rudziński, S. Suihkonen, H. Jussila, M. Knetzger, E. Meissner, A. Danilewsky, T. O. Tuomi and H. Lipsanen. Synchrotron radiation x-ray topography and defect selective etching analysis of threading dislocations in GaN. *Journal of Applied Physics*, Vol. 116, No 8, p. 083504, August 2014.

II S. Sintonen, S. Suihkonen, H. Jussila, A. Danilewsky, R. Stankiewicz, T.O. Tuomi and H. Lipsanen. Large area analysis of dislocations in ammonothermal GaN by synchrotron radiation x-ray topography. *Applied Physics Express*, Vol. 7, No 9, p. 091003, August 2014.

III S. Sintonen, S. Suihkonen, H. Jussila, H. Lipsanen, T.O. Tuomi, E. Letts, S. Hoff and T. Hashimoto. Defect structure of a free standing GaN wafer grown by the ammonothermal method. *Journal of Crystal Growth*, Vol. 406, p. 72-77, September 2014.

IV S. Sintonen, M. Ali, S. Suihkonen, P. Kostamo, O. Svensk, M. Sopanen, H. Lipsanen, C. Paulmann, T.O. Tuomi and M. Zajac. Synchrotron radiation X-ray topography and X-ray diffraction of homoepitaxial GaN grown on ammonothermal GaN. *Physica Status Solidi C*, Vol. 9, No. 7, p. 1630–1632, May 2012.

V S. Sintonen, M. Ali, P.T. Törmä, S. Suihkonen, P. Kostamo, O. Svensk, M. Sopanen, H. Lipsanen, C. Paulmann, T.O. Tuomi. X-ray diffraction study of

GaN grown on patterned substrates. *Physica Status Solidi C*, Vol. 8, No. 5, p. 1524–1527, March 2011.

VI P.T. Törmä, M. Ali, O. Svensk, S. Sintonen, P. Kostamo, S. Suihkonen, M. Sopanen, H. Lipsanen, M.A. Odnoblyudov and V.E. Bougrov. An investigation of structural properties of GaN films grown on patterned sapphire substrates by MOVPE. *Physica B: Condensed Matter*, Vol. 404, No. 23-24, p. 4911–4915, December 2009.

Author's Contribution

Publication I: "Synchrotron radiation x-ray topography and defect selective etching analysis of threading dislocations in GaN"

The Author wrote the manuscript, and designed and performed the experiments. Co-authors performed the defect selective etching, prepared the defect selective etching images and participated in recording the synchrotron topographs.

Publication II: "Large area analysis of dislocations in ammonothermal GaN by synchrotron radiation x-ray topography"

The Author wrote the manuscript, and designed and performed the experiments. Co-authors prepared the sample and participated in recording the synchrotron topographs.

Publication III: "Defect structure of a free standing GaN wafer grown by the ammonothermal method"

The Author wrote the manuscript, and designed and performed the experiments. Co-authors prepared the sample and participated in recording the synchrotron topographs.

Publication IV: "Synchrotron radiation X-ray topography and X-ray diffraction of homoepitaxial GaN grown on ammonothermal GaN"

The Author wrote the manuscript, and designed and performed the experiments. Co-authors prepared the sample and participated in recording the syn-

chrotron topographs.

Publication V: "X-ray diffraction study of GaN grown on patterned substrates"

The Author wrote the manuscript, and designed and performed the experiments. Co-authors prepared the samples, recorded the scanning electron microscopy image and participated in recording the synchrotron topographs.

Publication VI: "An investigation of structural properties of GaN films grown on patterned sapphire substrates by MOVPE"

The Author performed the high resolution x-ray diffraction measurements.

List of Abbreviations

AFM	Atomic force microscopy
ANKA	Ångströmquelle Karlsruhe
BPD	Basal plane dislocation
CCD	Charge coupled device
CL	Cathodo-luminescence
DESY	Deutsches Elektronen-Synchrotron
DORIS III	The storage ring Double Ring Store III at DESY
DSE	Defect selective etching
FWHM	Full width at half maximum
HASYLAB	Das Hamburger Synchrotronstahlungslabor
HRXRD	High resolution x-ray diffraction
HVPE	Hydride vapour phase epitaxy
LD	Laser diode
LED	Light emitting diode
MBE	Molecular beam epitaxy
MD	Misfit dislocation
MOVPE	Metallo organic vapour phase epitaxy
RGB	Red, green, blue
RSM	Reciprocal space map
SEM	Scanning electron microscopy
SR-XRT	Synchrotron radiation x-ray topography
TD	Threading dislocation
TED	Threading edge dislocation
TEM	Transmission electron microscopy
TMD	Threading mixed dislocation
TSD	Threading screw dislocation
XRD	X-ray diffraction

List of Symbols

$\mathbf{a_1}, \mathbf{a_2}, \mathbf{a_3}$	In plane crystal lattice unit vectors
a	In plane lattice constant, $a = \lvert\mathbf{a_i}\rvert$
$\mathbf{b}$	Burgers vector
b	Burgers vector magnitude
B	Bending magnet magnetic field
$\mathbf{b_1}, \mathbf{b_2}, \mathbf{b_3}$	Reciprocal space unit vectors
$\mathbf{c}$	Out of plane crystal lattice unit vector
c	Out of plane lattice constant $c = \lvert\mathbf{c}\rvert$ or the speed of light
d	Distance between crystallographic planes
D	Dislocation spacing
ΔL	Path difference of diffracted x-rays
E	Synchrotron beam particle energy
$\mathbf{g}$	Diffraction vector
$\hbar$	Reduced Planck's constant
$\mathbf{H}$	Reciprocal lattice vector
h, k, l	Miller indices
h, k, i, l	Miller-Bravais indices
I	Synchrotron beam current or x-ray intensity
$K_{5/3}$	Modified Bessel function of second kind and 5/3 fractional order
$\mathbf{k_0}$	Incident wave vector
$\mathbf{k_s}$	Scattered wave vector
$\mathbf{l}$	Dislocation line vector
m_0	Electron rest mass
$\mathbf{n}$	Diffracting plane normal
N	Defect density
q	Electron charge
t, t_{eff}	Crystal thickness, effective crystal thickness
$\mathbf{u}$	Displacement field of a dislocation
V	Unit cell volume

α	Lattice misorientation angle or fine structure coefficient
β_1, β_2	Incident and scattered x-ray beam angles with respect to the sample surface
γ	Relativistic quantity
ϵ_a, ϵ_c	In plane and out of plane lattice strain
$\lvert\Delta\epsilon_a\rvert$, $\lvert\Delta\epsilon_c\rvert$	In plane and out of plane strain variation
ϵ_p	Photon energy
ϵ_c	Critical photon energy
θ	Bragg angle of diffraction
λ	X-ray wavelength
μ	Linear attenuation coefficient
ϕ	Sample rotation about surface normal
Φ	Synchrotron spectral flux
ψ	Sample tilt about an in-plane axis
ω	Incident x-ray beam angle
ω_p	Photon angular frequency
ω_c	Critical photon angular frequency

1. Introduction

Gallium nitride (GaN) has been researched extensively due to its undisputed potential in the optoelectronic and the high power device industry. It is currently considered the best material choice for white light emitting diodes (LED) and is expected to significantly reduce future general lighting costs. GaN based blue and green lasers have also been commercialized, enabling smaller and more efficient laser projectors at a reduced cost. The robust nature and wide tunable range of optical properties has also generated interest in use of GaN in high power devices and solar cells.

For economic and previous technological reasons, GaN growth has practically been restricted to growth on foreign substrates. The former lack of a suitable substrate has limited the crystal quality and resulted in a high density of crystallographic defects. The defects impair the device perfomance and great effort has consequently been put into improving the crystal quality of GaN. Efforts to reduce the defect density in GaN include growth on patterned substrates and fabrication of free standing GaN wafers. Bulk GaN wafers have developed rapidly, and contemporary GaN wafers have a defect density too low for practical defect characterization using conventional techniques. To further improve the structural quality of low defect density GaN, accurate and effective characterization of the defect structure is essential.

In this thesis, the defect structures of free standing GaN wafers, homoepitaxial GaN films and heteroepitaxial GaN films grown on patterned substrates are characterized by synchrotron radiation x-ray topography (SR-XRT), x-ray diffraction (XRD) and defect selective etching (DSE). SR-XRT is used to identify individual defects, distinguish between defect types and characterize the defect structure of low defect density GaN over a large area. The fundamental properties of GaN, including the crystal structure, crystallographic defects and growth methods are discussed in chapter 2. A large part of the work relies on x-ray diffraction, and the necessary x-ray diffraction theory is reviewed in chapter 3. A

short introduction to synchrotron radiation, background on the SR-XRT measurement principle, defect contrast mechanisms in topographs and key aspects of screw dislocation topograph image simulation are presented in chapter 4. Defect selective etching is briefly reviewed in chapter 5. Selected results are presented in chapter 6, followed by the summary in chapter 7.

2. Fundamentals of GaN

2.1 GaN Overview

As a result of its direct wide bandgap, gallium nitride based semiconductor devices have great potential as high efficiency, short wavelength light emitters. The bandgap size and therefore the emission wavelength may be tuned by incorporating group III elements indium and aluminium, allowing the (InAl)GaN material system to emit light from ultra violet to near red. The material system is thus considered one of the most important in optoelectronics, motivating extensive research in the field of III-nitrides.

Early InGaN-based blue light emitting diodes (LED) were demonstrated in 1994 by Nakamura *et al.* [1] and have since been successfully commercialized. The biggest potential market for short wavelength LEDs is white light solid state lighting. White light emission is achieved by either combining light outputs of red, green and blue LEDs or from a short wavelength blue or violet LED coated with a phosphor. The phosphor coating converts the short wavelength blue or violet light to longer wavelengths and emits white light. The current efficiency of InGaN LEDs is only a fraction of the theoretical efficiency and, for instance, advances in solid state lighting is expected to save 1100 TWh worldwide in electricity by 2025 [2]. A further advantage of the InGaN LED is its non-toxicity and long lifetime.

The short wavelength of the blue InGaN-based laser diode (LD) has enabled denser packing of data on Blu-ray disks compared to traditional DVDs, operated with longer laser wavelengths [3]. Osram and Nichia have recently introduced InGaN-based LDs emitting in the green [4, 5]. This opens up the possibility to use high efficiency, small size LDs in RGB-projectors with InGaN LDs as blue and green light sources and AlGaInP LDs as the red light source. Semiconductor lasers exciting a yellow phosphor are also finding new applications as

BMW is starting series production of car headlights using Osram lasers, with production start due in late 2014 [6, 7].

The direct, wide and tunable bandgap of GaN is also well suited for solar cell applications. The achievable InAlGaN bandgap range covers most of the solar spectrum. GaN solar cells are theoretically very efficient and GaN solar cells with much improved efficiency have recently been demonstrated [8].

GaN is mechanically robust, chemically stable, withstands high temperatures and high voltages and is consequently used in high power electronics [9]. GaN-based power electronics are advantageous in the automotive industry, owing to its great reliability and stability [10]. Other power applications include radio frequency power amplifiers and devices [11].

Although GaN has tremendous potential in a variety of applications, the sub ideal material quality is limiting GaN based device performances. GaN is commonly grown on foreign substrates and the mismatch of thermal expansion and lattice constants results in a high number of crystal defects [12]. The defects have a negative impact on the optical and electrical properties of the semiconductor. Defects act as non-radiative recombination centres, increase leakage current and obstruct charge carriers, resulting in reduced light output in optoelectronic devices [13]. Crystalline defects also hinder high current density operation of devices. While this may be acceptable in low power applications, for instance, flash lights and signal LEDs, it is detrimental for applications that require high current density, i.e. general lighting, laser diodes and high power electronics.

While many heteroepitaxial growth methods aimed at reducing crystalline defects have been proposed, best structural quality GaN has been achieved with bulk growth methods [14]. Great effort has been put into developing bulk GaN growth methods, including the Na-flux method [15, 16], high- pressure solution growth [17–19], hydride vapour phase epitaxy (HVPE) [20, 21], ammonothermal growth [22–25] and a combination of the two latter methods [26, 27]. Of these methods, the ammonothermal GaN growth is a scalable and efficient growth method for high quality bulk crystals [28]. Bulk GaN is expected to improve LED efficiency due to already demonstrated reduced non-radiative recombination, leakage current, improved thermal conductivity and increased lifetime [29]. Laser diodes, solar cells and power devices benefit from the reduced defect density similarly, and the power devices benefit additionally from elevated carrier mobility and higher breakdown voltage. The drawback of bulk GaN substrates is their hitherto high cost, which limits their use to high end applications, e.g. high power lasers, only. It has however been reported that

ammonothermal GaN could be cost effective in white light LEDs as well [30].

The high quality of bulk GaN substrates impedes the defect characterization by conventional methods, such as transmission electron microscopy (TEM), atomic force microscopy (AFM), cathodo-luminescence (CL) and scanning electron microscopy (SEM). The small probe size ≤ 100 μm is common to all electron beam methods, while the typical practical AFM measurement range is even smaller. The probe size is thus too small for characterization of state of the art crystals with defect density as low as 5×10^3 cm^{-2} [31]. Recording of representative data is very tedious and time consuming even from crystals with higher defect density 1×10^5 cm^{-2}. X-ray based techniques have larger probe sizes and are better suited for low defect density material characterization. Synchrotron radiation x-ray topography is particularly befitting, since it can probe the defect structure over several square centimetres.

2.2 Crystal Structure

Crystalline materials have atoms arranged periodically in all three dimensions. The regularly positioned atoms form a unit cell which is the smallest measure that can be repeated to maintain the crystal symmetry [32]. Although there are many different unit cells, this work will focus exclusively on GaN arranged in the hexagonal wurtzite lattice. The hexagonal crystal structure has sixfold symmetry as shown in figure 2.1. One unit cell has been drawn with solid lines and includes positions of Ga atoms (red) and N atoms (blue) as well as nearest neighbour bonds indicated by green lines. Two additional unit cells are needed to display the hexagonal symmetry and are outlined with dashed lines in figure 2.1.

The unit cell is defined by three lattice vectors and the magnitudes of the vectors are called lattice constants. Although three vectors are sufficient to define a lattice in three dimensions, four vectors are often used in hexagonal materials to underline crystallographic symmetry. In the four index notation lattice vectors $\mathbf{a_1}$, $\mathbf{a_2}$ and $\mathbf{a_3}$ all lie in the basal plane, while the fourth unit vector $\mathbf{c}$ is perpendicular to the basal plane. The angle between $\mathbf{a_1}$, $\mathbf{a_2}$ and $\mathbf{a_3}$ is 120° and it follows that $\mathbf{a_3} = \mathbf{a_2} - \mathbf{a_1}$. The wurtzite structure has two unit vector lengths $|\mathbf{a_1}| = |\mathbf{a_2}| = |\mathbf{a_3}| = a$ and $|\mathbf{c}| = c$. The directions and magnitudes of the lattice vectors are also shown in figure 2.2. The Ga-polar unit cell in figure 2.1 has Ga atoms located at $(0,0,0)$ and $(\frac{1}{3},\frac{1}{3},\frac{1}{2})$, expressed in fractions of the wurtzite lattice vectors. The u parameter is defined as the nearest neighbour distance divided by the lattice parameter c, and is $\frac{3}{8}$ for an ideal wurtzite lattice. The N

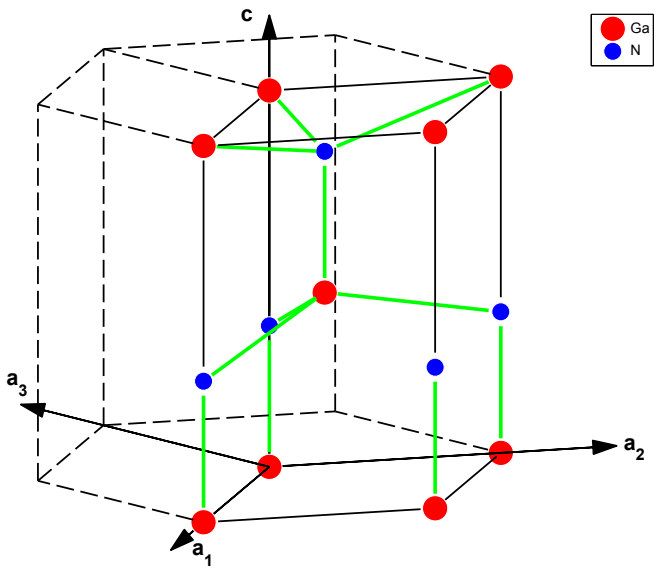

Figure 2.1. The hexagonal wurtzite lattice. One Ga-polar unit cell is drawn with solid lines and two unit cells with dashed lines. Atomic positions of Ga and N atoms are marked with red and blue spheres, respectively. Nearest neighbour bonds are marked in green.

atoms in the ideal lattice in figure 2.1 should therefore be located at $(0,0,\frac{3}{8})$ and $(\frac{1}{3},\frac{1}{3},\frac{7}{8})$, in hexagonal lattice coordinates. Real crystals have usually a slightly larger u parameter, and for GaN the experimental value is 0.377, whereas the ideal value is $\frac{3}{8} = 0.375$ [33].

Due to inherent anisotropy of crystals, the concept of crystallographic directions and crystallographic planes is used. The directions and planes are described by three Miller indices hkl or four Miller-Bravais indices $hkil$ [32]. A crystallographic plane that intersects the coordinate axes at (x_0, y_0, z_0) has Miller indices $(hkl) = n \times (\frac{1}{x_0}, \frac{1}{y_0}, \frac{1}{z_0})$, where $n \in \mathbb{Z}_+$ is chosen to yield the smallest integers (hkl). In hexagonal crystals, the four index notation is often used, where $i = -h - k$. A negative index is written $\bar{i}$. Crystallographic directions are written inside brackets $[hkil]$ and equivalent directions $\langle hkil \rangle$, whereas crystallographic planes are expressed with parentheses $(hkil)$ and equivalent planes $\{hkil\}$. Four index notation was used in all publications except V and VI, where the three index notation $[hkl]$ was used. It should be noted that $[100] \neq [10\bar{1}0]$. The three index and four index crystallographic directions are shown in figure 2.2. In GaN the equivalent $\langle 11\bar{2}0 \rangle$ directions are referred to as the a-directions and the corresponding equivalent crystallographic planes $\{1\bar{1}\bar{2}0\}$ as a-planes. The m-directions are $\langle 1\bar{1}00 \rangle$ and m-planes $\{1\bar{1}00\}$ [33].

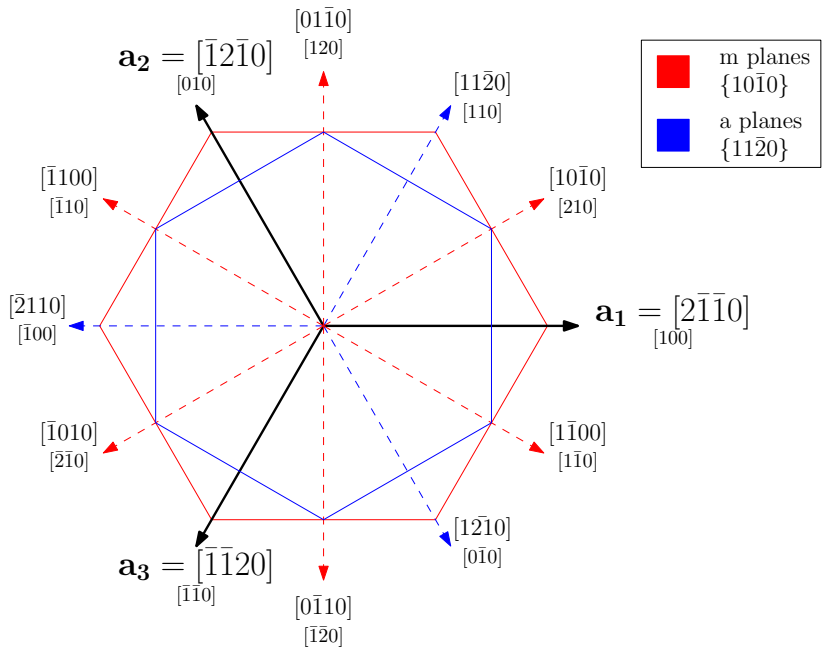

Figure 2.2. Crystallographic planes and directions in three and four index notation for a hexagonal crystal structure.

GaN is electrically polar along the [0001] direction. The polarization is a sum of spontaneous polarization and piezoelectric polarization. The spontaneous polarization is caused by a deviation from the ideal value of the u parameter and the piezoelectric polarization by presence of lattice strain [34]. The c-plane normal vector is defined as [0001] and the $-c$-plane normal vector [000$\bar{1}$]. The unit cell in figure 2.1 is Ga-polar with [0001] pointing upwards. The reversal of the Ga and N atomic positions would render the structure N-polar. GaN has mostly been grown on c-plane substrates, but the negative effect of polarization on device performance has encouraged and escalated research in nonpolar and semipolar GaN substrates. The nonpolar m- and a-planes are perpendicular to the polar c-plane, whereas the semipolar planes are angled to the c-plane. Only c-plane GaN was discussed in the publications of this thesis.

2.3 Dislocations in Crystals

The atoms in real crystals are not perfectly ordered and local deviations from the perfect lattice are called crystalline defects. Crystalline defects can be point, line, surface or volume defects [35]. Dislocations are one dimensional line de-

fects and differ from other types of lattice defects by their long range influence on the surrounding lattice. Dislocations are defined by a line vector **l** and a Burgers vector **b** [36, 37]. The Burgers vector describes the magnitude and direction of the lattice disturbance whereas the line vector describes the propagation direction of the dislocation. Since dislocations displace a part of the lattice, the Burgers vector can not be arbitrary and usually equals one of the lattice vectors.

There are three elemental types of dislocations; the screw dislocation, the edge dislocation and the mixed dislocation. The mixed dislocation is a combination of the screw and the edge dislocations and can not strictly be considered an independent type of dislocation, but is often treated as such as it is ubiquitous in GaN. Screw dislocations have parallel Burgers vector and line vector, whereas the edge dislocation has its Burgers vector perpendicular to its line vector. The edge and screw dislocations in an arbitrary lattice are illustrated schematically in figure 2.3. The edge dislocation is formed by insertion of an extra half plane of atoms, shown in red in figure 2.3(a). The lattice planes around the edge dislocation are forced to bend away from the excess half plane and cause the lattice to be distorted. The screw dislocation follows the shape of a helicoid, as shown in figure 2.3(b). Part of the lattice is shifted down one lattice vector, causing the lattice planes to distort and form a spiral stair case around the dislocation core.

Since dislocations displace the whole lattice in one dimension, they cannot start or end inside a crystal. Dislocations must have start and end points at surfaces, other defects, or form closed loops [38]. The surfaces can be internal, e.g. a grain boundary, or external, i.e. the face of the crystalline material. The defects can be other dislocations or various kinds of inclusions, such as foreign particles, liquid inclusions and bubbles, as long as it interrupts the lattice sequence [39]. Analogous to Kirchoff's law of electrical current, the sum of all Burgers vectors at a dislocation node equals zero, $\sum_i \mathbf{b_i} = \mathbf{0}$, and opposite dislocations may therefore annihilate. Another important property of the dislocation is its ability to move through the crystal and is the reason for plasticity of crystalline materials [40]. The dislocations move in a slip plane which is a plane containing both the dislocation line vector and Burgers vector.

In GaN, threading dislocations are dislocations with a line vector perpendicular to the sample surface. The dislocations thread through the active device layers and protrude the sample surface with detrimental consequences. Threading dislocations have negative impact on optical and electrical performance of GaN devices and great effort is therefore being put into reducing threading dislo-

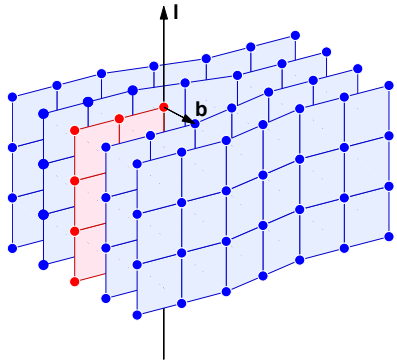

(a)

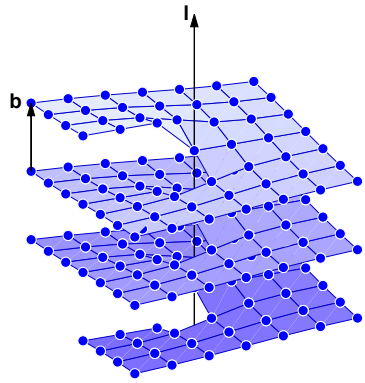

(b)

Figure 2.3. Schematic illustrations of the edge dislocation (a) and the screw dislocation (b). The screw dislocation has parallel line vector **l** and Burgers vector **b**, while the vectors are perpendicular in the edge dislocation. The extra half plane of the threading edge dislocation is shown in red.

cation density in GaN. All samples studied in this thesis were c-plane GaN and hereafter threading dislocations will denote dislocations with line vector $\mathbf{l} = [0001]$. The Burgers vectors of threading screw, edge and mixed dislocations are $\mathbf{b}_{\text{screw}} = [0001]$, $\mathbf{b}_{\text{edge}} = \frac{1}{3}[11\bar{2}0]$ and $\mathbf{b}_{\text{mixed}} = \frac{1}{3}[11\bar{2}3]$. The magnitudes are therefore $|\mathbf{b}_{\text{screw}}| = c$, $|\mathbf{b}_{\text{edge}}| = a$ and $|\mathbf{b}_{\text{mixed}}| = a + c$.

In addition to the edge, screw and mixed dislocations, super screw dislocations and micropipes which are large screw type dislocations have been reported in SiC [41–44]. These dislocations have large Burgers vectors $\mathbf{b} = n\mathbf{c}$, where n is an integer and $\mathbf{c}$ the lattice vector, and they are essentially screw dislocations with multiple Burgers vectors. Although there is some ambiguity in the terminology, dislocations with $\mathbf{b} \geq 2\mathbf{c}$ are generally called super screw dislo-

cations and super screw dislocations with hollow cores are termed micropipes [45]. Whether the core is closed or not depends on the size of the Burgers vector. In 4H SiC, for instance, the dislocation has an open core when $\mathbf{b} \geq 3\mathbf{c}$ and a closed core when $\mathbf{b} \leq 2\mathbf{c}$ [46, 47].

Basal plane dislocations (BPD) are analogous to threading dislocations but are confined to the basal plane of the crystal [48]. It is important to distinguish BPDs from TDs, since in *c*-plane GaN, dislocations in the basal plane do not propagate in the *c*-direction and are therefore less harmful to polar GaN device performance. BPDs are however harmful to semipolar and nonpolar GaN devices. Misfit dislocations (MD) are dislocations created by a mismatch between two epitaxial materials [49]. MDs form one or two dimensional MD arrays since by definition an extra lattice plane is inserted with a periodic spacing to accommodate the mismatch. BPDs and MDs were discussed in publication III.

2.4 GaN Growth

Due to earlier lack of low cost native substrates, GaN has commonly been grown on foreign substrates, e.g. sapphire, SiC and Si, by molecular beam epitaxy (MBE), hydride vapour phase epitaxy and metallo organic vapour phase epitaxy (MOVPE) [50]. In this work, only bulk crystals grown by the ammonothermal method and GaN films grown by MOVPE on sapphire were studied. These methods will be reviewed briefly.

MOVPE is an epitaxial growth technique, i.e. the atomic arrangement of the substrate crystal surface is reproduced in the grown material. In MOVPE, the thermally decomposed metalorganic precursor gas trimethylgallium (TMGa) and gaseous ammonia (NH_3) react at the sample surface and form crystalline GaN [51, 52]. Figure 2.4 shows a schematic of the MOVPE reactor design. The group III and group V precursors are transported in separate lines into the reaction chamber and are distributed uniformly by the close coupled showerhead. The reactor design prevents precursors from reacting away from the susceptor surface, which significantly reduces premature reactions. The susceptor holds three 2 inch wafers and is heated to provide a typical growth temperature close to 1000 °C.

C-plane GaN and sapphire have a ≈ 16 % lattice mismatch and 80 % thermal mismatch, which hinders direct MOVPE growth of GaN on sapphire [52]. The two step method overcomes this by using an aluminium nitride (AlN) or GaN nucleation layer grown at a lower temperature [54]. The structural quality of

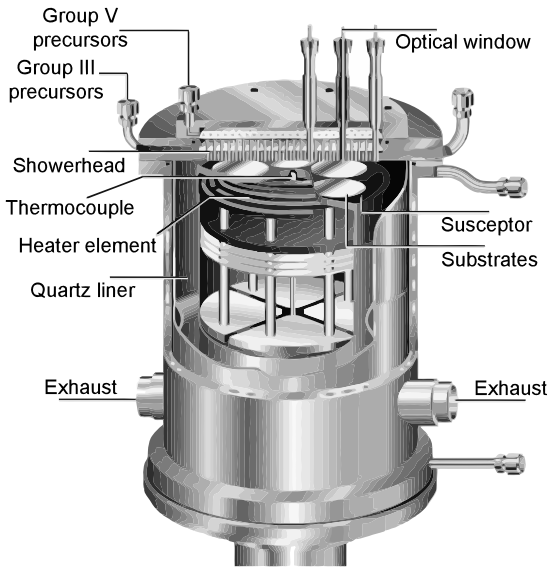

Figure 2.4. Schematic representation of the metallo organic vapour phase epitaxy reactor. Image from [53].

the following GaN layer is greatly improved by the two step method. MOVPE grown GaN samples were studied in publications IV, V and VI. In publication VI, the sapphire substrate was patterned by etching to investigate the effects of pillar structure and hole structure on the heteroepitaxial GaN. The GaN layers in publication V were grown on patterned GaN/sapphire templates. The templates consisted of MOVPE grown GaN layers on sapphire, and the GaN layers were patterned to have a holey structure with varying hole diameter and hole to hole distance. MOVPE growth details of publication V can be found in references [55–57]. The GaN epilayer in publication IV was grown by MOVPE on an ammonothermal GaN substrate.

The ammonothermal method is analogous to the hydrothermal method used to mass produce quartz, except that in the ammonothermal method ammonia is used as a solvent instead of water [58]. The growth process is shown in figure 2.5: GaN feedstock is dissolved in the upper part of the autoclave and transported to the seed crystals in the bottom part of the autoclave by convection, and crystallization occurs because of supersaturation of the solution [58]. Mineralizers are used to enhance GaN solubility in ammonia and determine whether the process environment is basic or acidic and if the resulting crystal structure is cubic or hexagonal. The temperature difference between the GaN seed and feedstock regions is positive in the ammonobasic regime and negative in the ammonoacidic regime. Ammonothermal crystals studied in publications I, II

and IV were grown under ammonobasic conditions with alkali ($LiNH_2$, $NaNH_2$ or KNH_2) mineralizers [59]. The crystal in publication III was grown with a sodium based mineralizer in a basic ambient [60].

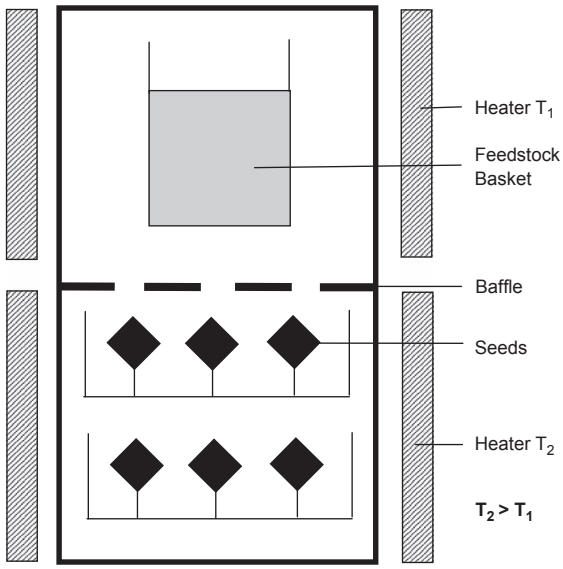

Figure 2.5. Schematic representation of the ammonothermal GaN growth method. GaN feedstock is dissolved in ammonia and transported to the seed crystals by convection. The dissolved GaN crystallizes at the seed surface. Image from [58].

3. X-ray Diffraction

3.1 Bragg's Law

X-rays are electromagnetic radiation with wavelengths between those of gamma rays and ultraviolet light. The x-ray wavelengths used in diffraction experiments of crystalline materials are in the order of 1 Å. Wilhelm Röntgen is credited for the discovery of x-rays in 1895 [61] and the field of x-ray crystallography developed quickly after. X-rays are generally non destructive and enable structural characterization of crystalline materials at an atomic level.

As a result of the periodic stacking of atoms, crystallographic planes in a given direction are theoretically spaced equally apart. For a hexagonal structure, the spacing d_{hkl} of (hkl) planes is [62]:

$$d_{hkl} = \sqrt{\frac{3}{4\{\frac{h^2+k^2+hk}{a^2} + \frac{3l^2}{4c^2}\}}} \tag{3.1}$$

where a and c are lattice constants and hkl the Miller indices. Bragg's law for diffraction [63]

$$n\lambda = 2d\sin\theta \tag{3.2}$$

where λ is the x-ray wavelength and θ the diffraction angle, states that constructive interference of x-rays occurs whenever the difference in x-ray path length is an integer multiple of the wavelength. The integer n can in practice always be chosen to be 1 by substituting $d' = dn$ into equation (3.2). The diffraction geometry based on ray optics is illustrated in figure 3.1, where the incident beams are depicted in blue and the scattered beams in green. It is seen that for a given Bragg angle θ and distance between lattice planes d, the path difference $\Delta L = 2d\sin\theta$ or multiples thereof.

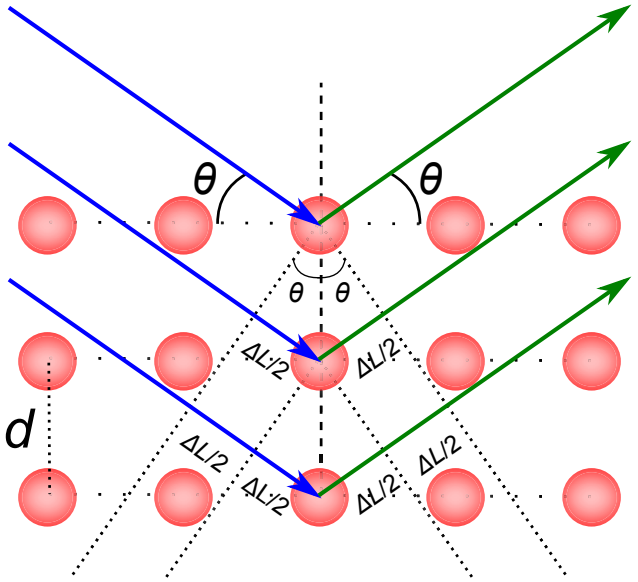

Figure 3.1. Geometric representation of Bragg's law. The incident x-rays are drawn in blue and scattered x-rays in green. The distance between the horizontal rows of atoms (red) is d. The path difference ΔL for a given Bragg angle θ is always $2d\sin\theta$ or a multiple thereof.

3.2 High Resolution X-Ray Diffraction

High resolution x-ray diffraction (HRXRD) was used in all publications. Figure 3.2 shows a schematic drawing of the used HRXRD setup. In HRXRD, the divergent x-ray beam, dark blue triangle in figure 3.2, is collimated by the graded multilayer parabolic x-ray mirror and is passed through the four-crystal Bartels monochromator [64]. The monochromator allows through only a narrow wavelength bandwidth in approximately a single direction, since x-rays need to undergo a quadruple diffraction event in order to pass through. The x-rays are then diffracted by the sample into the detector via the analyzer. The diffracted x-ray beam is shown in dark green in figure 3.2. The goniometer angles ω, 2θ, ϕ and ψ with rotation planes are shown in lighter shades of blue, green, red and yellow, respectively. The angle 2θ is defined as the angle between the diffracted beam and the extended incident beam. The analyzer is in concept similar to the monochromator as x-rays undergo two additional diffraction events before reaching the detector, thus improving the angular resolution and narrowing the accepted wavelength distribution. The practical resolution of the used HRXRD setup is ≈ 10 arc seconds, while the monochromator full width at half maximum (FWHM) is ≤ 14 arc seconds and the monochromator acceptance angle 12 arc seconds.

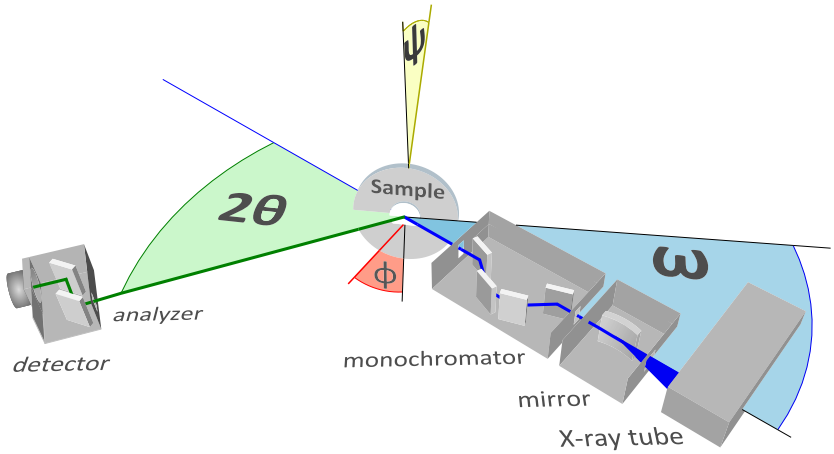

Figure 3.2. High resolution XRD setup. The incident x-ray beam (blue) is collimated by the parabolic x-ray mirror and x-rays with approximately only one wavelength and direction are diffracted through the monochromator to the sample. The scattered x-rays (green) are monochromated again by the analyzer before reaching the detector.

3.3 ω Rocking Curve and 2θ-ω Measurements

In ω rocking curve measurements, the detector is kept stationary while the incident angle ω is rocked around the maximum position of intensity. This is one of the most common measurement types and the ω peak broadening is used for a quick overview of the crystal quality. Peak broadening is caused by dislocations, instrumental broadening, lattice strain, limited correlation length and wafer curvature [65]. Crystalline defects distort the surrounding lattice and cause a spread in the incident angle ω, for which Bragg's law of diffraction is satisfied. Crystalline defects impact the rocking curve width differently, depending on which lattice planes are used for diffraction. The invisibility criteria, discussed later in section 4.3, predict that symmetric (000l) rocking curves are unaffected by pure threading edge dislocations, whereas asymmetric (hki0) rocking curves are unaffected by pure threading screw dislocations. The study of rocking curves recorded with symmetric and asymmetric diffraction conditions therefore allows to discriminate between different types of dislocations. Symmetric and asymmetric ω rocking curve measurements were utilized in publications II, III, IV and VI to distinguish between different types of crystalline defects.

In 2θ-ω measurements, the detector angle and incident angle are scanned maintaining the condition $2\theta/\omega = 2$. The measurement probes the distance between lattice planes, and lattice constants a and c can be calculated from at least two measurements by combining equations (3.1) and (3.2). The lat-

tice constant c in publication II was determined as an average value from four (0004) and four (0006) $2\theta-\omega$ scans rotated 90° about the c-axis between each measurement. The average value c was then used in conjunction with three $(10\bar{1}5)$ and three $(10\bar{1}6)$ scans, rotated 120° about the c-axis, to obtain the value for a. Measurements were corrected taking into account that x-rays have a refractive index below 1 [66, 67].

Lattice strain is defined as the difference in lattice constants between the sample and the substrate or reference value. The in plane strain ϵ_a and out of plane strain ϵ_c are calculated from equation (3.3)

$$\begin{aligned} \epsilon_a &= \frac{a-a_0}{a_0}\times 100\% \\ \epsilon_c &= \frac{c-c_0}{c_0}\times 100\% \end{aligned} \tag{3.3}$$

where a and c are the measured lattice constant values and a_0 and c_0 are the lattice constants of the substrate or reference sample. Due to earlier lack of native substrates, there is significant scatter in reported values of the GaN lattice constants [68, 69]. The precise lattice constants of unstrained GaN is still under debate but recent reports on bulk GaN lattice parameters exhibit less scatter [66, 70]. For this reason, an accurate absolute strain value cannot be computed from equation (3.3) and reference sample lattice constant values a_0 and c_0 were used in publication VI to assess strain relaxation of GaN grown on patterned sapphire substrates. Strain variation within a sample was calculated in publication III also using equation (3.3).

3.4 Reciprocal Space

The reciprocal space is defined by three unit vectors. The unit vectors are related to real space according to equation (3.4) [71]

$$\mathbf{b}_i = 2\pi\frac{(\mathbf{a}_j\times\mathbf{a}_k)}{(\mathbf{a}_1\times\mathbf{a}_2)\cdot\mathbf{a}_3} = \frac{2\pi}{V}(\mathbf{a}_j\times\mathbf{a}_k),\ i,j,k\in\{1,2,3\}, \tag{3.4}$$

where $\mathbf{b}_i$ is the reciprocal space unit vector, $\mathbf{a}_i$ the real space unit vector in direction i and V the volume of the unit cell. It follows from equation (3.4) that the reciprocal space vector length is the reciprocal of the corresponding real space lattice vector length and that $\mathbf{b}_i$ is always perpendicular to $\mathbf{a}_j$ and $\mathbf{a}_k$.

The reciprocal lattice is a discrete form of the reciprocal space. A reciprocal lattice point or vector is an integer coefficient linear combination of the reciprocal space unit vectors. Equation (3.5) displays the relationship between the reciprocal lattice vector $\mathbf{H}_{hkl}$ and the Miller indices (hkl)

$$\mathbf{H}_{hkl} = h\mathbf{b}_1 + k\mathbf{b}_2 + l\mathbf{b}_3,\ h,k,l\in\mathbb{Z} \tag{3.5}$$

and shows that a set of lattice planes (hkl) in real space corresponds to a reciprocal lattice point $\mathbf{H}_{hkl}$.

Diffraction from (hkl) planes in reciprocal space is described by the scattering vector $\mathbf{H}_{hkl} = \mathbf{k}_s - \mathbf{k}_0$, where $\mathbf{k}_0$ is the incident wave vector and $\mathbf{k}_s$ is the diffracted wave vector [32]. It can be shown, that the scattering vector is related to Bragg's law, equation (3.2), according to equation (3.6) [62].

$$|\mathbf{H}_{hkl}| = \frac{2\sin(\theta)}{\lambda} = \frac{1}{d_{hkl}}, \tag{3.6}$$

Figure 3.3 shows a schematic drawing of the Ewald's sphere for monochromatic x-rays [72]. The Ewald's sphere links diffraction in real space to diffraction in reciprocal space. The example displays diffraction from the (114) planes of an arbitrary crystal and shows the relationship between $\mathbf{k}_0$, $\mathbf{k}_s$, $\mathbf{H_{114}}$ and the diffracting plane normal vector $\mathbf{n}$. The reciprocal lattice origin is chosen to coincide with the starting point of $\mathbf{H_{114}}$ and is illustrated in red colour in figure 3.3. The reciprocal lattice point (114) is shown green in figure 3.3. Vectors $\mathbf{k}_0$ and $\mathbf{k}_s$ have lengths $|\mathbf{k}_0| = |\mathbf{k}_s| = 1/\lambda$ and the Ewald's sphere is traced by rotating these vectors. Diffraction is only possible when a reciprocal lattice point coincides with the Ewald's sphere. It should be noted that figure 3.3 depicts the Ewald's sphere for monochromatic radiation and is valid for a standard laboratory setup, but not for polychromatic radiation, such as synchrotron radiation. Each wavelength will trace an Ewald's sphere of different radius and in the case of a continuous wavelength distribution, the Ewald's sphere effectively becomes a hollow sphere with wall thickness corresponding to the wavelength distribution. It is seen from figure 3.3 that for a large enough wavelength distribution the sphere wall is sufficiently thick to coincide with most reciprocal lattice points, enabling simultaneous diffraction from the corresponding lattice planes.

Reciprocal space maps (RSM) are two dimensional slices of a reciprocal lattice point. They are formed by recording a series of $2\theta - \omega$ scans and offsetting the ω value between each scan. The resulting image consist of diffracted intensity distribution as a function of both ω and $2\theta - \omega$, and the RSM therefore combines, and adds to, the information of ω-rocking curves and $2\theta - \omega$ scans. The RSM maximum is broadened by wafer curvature, different types of defects, small crystal misorientation, limited crystal size, composition gradients and lattice strain, i.e. lattice parameter variation [65]. The exact lattice parameters can in principle be determined from a single asymmetric RSM, but high resolution and rapid data collection are mutually exclusive. RSMs are therefore used for an overview of crystal quality, and they are especially convenient in the study

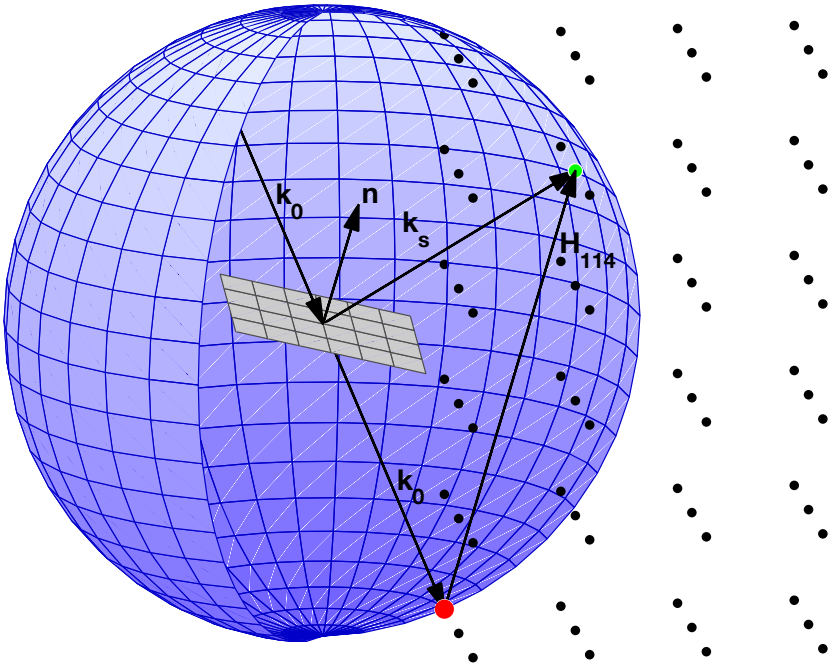

Figure 3.3. Monochromatic diffraction from (114) planes, Ewald's sphere and reciprocal space. The scattering vector $\mathbf{H}_{\mathbf{114}}$ is defined by the incident and diffracted wave vectors $\mathbf{k}_0$ and $\mathbf{k}_s$. The reciprocal lattice origin is marked in red and the reciprocal lattice point (114) in green.

of strained heteroepitaxial structures. RSMs were utilized in publications III and V.

4. Synchrotron Radiation X-Ray Topography

4.1 Synchrotron Radiation

The synchrotron was originally developed for research in high energy particle interaction with matter, but was found to emit electromagnetic radiation with a continuous wavelength spectrum, very low divergence and high brilliance [73]. These are extremely desirable qualities in the study of defects in semiconductors, and researchers started using the synchrotron in a parasitic manner, i.e whenever synchrotron radiation was made available by other experiments.

Figure 4.1 shows a schematic drawing of a synchrotron facility akin to the Ångströmquelle Karlsruhe (ANKA) in Karslruhe, Germany, where topography measurements for publications I and II were recorded [74, 75]. Synchrotron measurements for publications III, IV, V and VI were performed using the Double Ring Store (DORIS) III storage ring at Hamburger Synchrotronslabor am Deutschen Elektronen-Synchrotron (HASYLAB-DESY) in Hamburg, Germany. In figure 4.1, electrons are first accelerated to 53 MeV in the microtron, and then boosted to 500 MeV prior to injection into the storage ring. Some synchrotron facilities, for instance DORIS III, use positrons instead of electrons and differing means of initial particle acceleration. The particles are accelerated further in the storage ring to velocities near the speed of light. The electron paths, shown blue in figure 4.1, are modified by bending magnets, shown red in figure 4.1, to achieve a quasi circular path.

The charged particles are decelerated in the curved parts of the storage ring, emitting soft x-rays in a narrow cone (depicted green in figure 4.3) in the tangential directions [76]. This radiation is called synchrotron radiation. The spectrum of the emitted x-rays may be modified by undulators or wigglers, which are insertion devices with periodic magnet structures that accelerate and decelerate the particles to achieve the desired energy distribution.

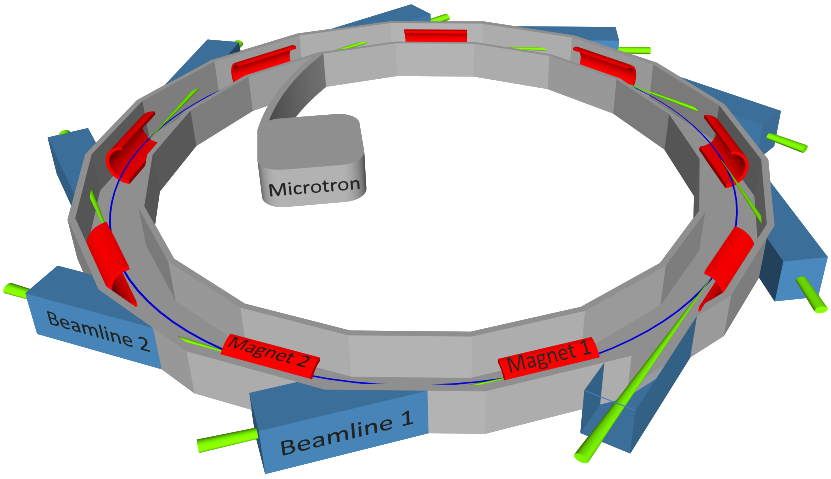

Figure 4.1. Schematic representation of a synchrotron light source. Particles are first accelerated to a moderate energy in the microtron and then injected into the storage ring where they are accelerated to velocities near the speed of light. Bending magnets (red) keep the particle path (blue) quasi circular. The decelerating charged particle in a magnet field emits synchrotron radiation in a tangential narrow cone (green). The experiments are conducted at beamlines.

The topography beamlines at ANKA and HASYLAB-DESY use the synchrotron radiation emitted by bending magnets. The bending magnets emit a continuous and polychromatic radiation, a white beam. If needed, a monochromatic beam can be achieved by selecting a single wavelength from the white beam using a monochromator. Some properties of the storage rings ANKA and DORIS III are listed in table 4.1 [77, 78]. The critical energy ϵ_c and spectral photon flux Φ are key figures used to describe a synchrotron light source. The critical energy is defined as the photon energy which divides the radiation spectrum in two halves of equal power [79, 80]. The critical energy ϵ_c of a bending magnet is calculated as [81]

$$\epsilon_c = \frac{2\hbar q}{m_0^3 c^4} E^2 B, \tag{4.1}$$

where $\hbar$ is the reduced Planck's constant, q the electron charge, m_0 the electron rest mass, c the speed of light, E the particle energy and B the magnet magnetic field of the bending magnet. The spectral photon flux Φ is often ambiguously expressed in several different units and here the definition of photons $\times$ s^{-1} $\times$ 0.1% BW^{-1} $\times$ mrad^{-1}, i.e. photons per time unit, 0.1% energy bandwidth ($\Delta\epsilon_p/\epsilon_p = 0.001$) and horizontal angle is used. The spectral flux of a bending magnet source is calculated by equation (4.2) [82, 83]

$$\Phi = \frac{\sqrt{3}}{2\pi} \alpha\gamma \frac{\Delta\omega_p}{\omega_p} \frac{I}{q} \frac{\omega_p}{\omega_c} \int_{\frac{\omega_p}{\omega_c}}^{\infty} K_{5/3}(y) dy. \tag{4.2}$$

Table 4.1. Properties of ANKA and DORIS III storage rings [77, 78].

Property	Unit	ANKA	DORIS III
Particle		Electron	Positron
Circumference	[m]	110	290
Particle energy E	[GeV]	2.50	4.45
Bending magnet field B	[T]	1.5	1.2
Particle beam current I	[mA]	180	140
Critical energy ϵ_c	[keV]	6	16
Peak photon flux Φ	$[\frac{\text{photons /s}}{0.1\%\text{BW}\times\text{mrad}}]$	7.9×10^{12}	1.4×10^{13}

In equation (4.2), $\alpha = 1/137$ is the fine structure coefficient, $\gamma = E/m_0c^2$ the relativistic quantity, $\Delta\omega_p/\omega_p = \Delta\epsilon_p/\epsilon_p = 0.001$ the energy and angular frequency bandwidth and I the beam current. The photon angular frequency is $\omega_p = \epsilon_p/\hbar$ and $K_{5/3}$ denotes the modified second order Bessel function.

The spectral fluxes of the bending magnets in DORIS and ANKA were calculated using equation (4.2) and parameters from table 4.1. The calculated curves are shown in figure 4.2 along with the critical energies for both storage rings. As seen from figure 4.2, ANKA has a spectrum with softer x-rays. The wavelengths used in topography are usually close to 1 Å and therefore have energies around 12.4 keV. The lower energy spectrum of the ANKA storage ring is beneficial in topography measurements, since high energy photons degrade the resolution through harmonic blurring.

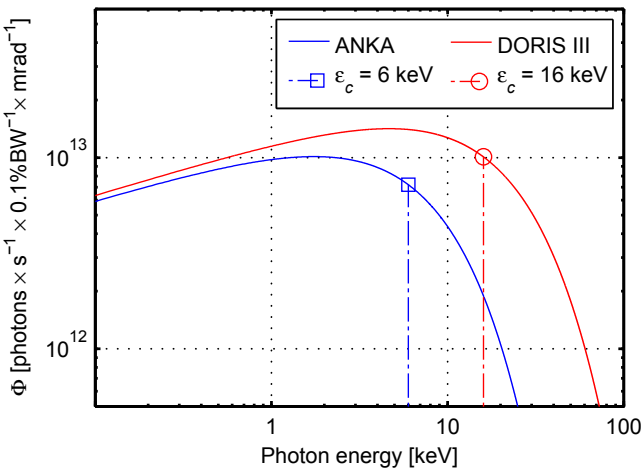

Figure 4.2. Calculated photon fluxes from the bending magnets at ANKA and DORIS III per 0.1% bandwidth and horizontal acceptance angle. The critical energies ϵ_c divide the spectra in two halves of equal radiated power.

4.2 Fundamentals of Synchrotron Radiation X-Ray Topography

In x-ray topography a crystal is irradiated with an appreciable size x-ray beam and the two dimensional spatial intensity distribution of the diffracted beam is recorded [84]. The recording media is usually an x-ray sensitive film or plate, although charge coupled device (CCD) cameras are also used. High resolution x-ray films have a spatial resolution of < 1 μm and the CCD camera ≈ 9 μm [77]. Although digital detection has many advantages, such as low noise and easy image processing, the x-ray film is still widely used, since it allows simultaneous recording of several diffraction spots in white beam topography. The x-ray film provides better resolution without the need of tedious detector alignment.

The dislocation density detection limit of SR-XRT is often estimated as $\approx 1 \times 10^5$ cm^{-2}. This is however not a fixed value limited by the resolution of the measurement equipment, but rather an estimation based on overlap of lineshaped dislocation images. As an example, at normal conditions at HASYLAB, the divergence limited horizontal resolution is $r_x = 4$ μm and the vertical resolution is $r_z = 1$ μm [85]. The divergence therefore limits the detection of sub micrometer sized features to $N \approx (r_x \times r_z)^{-1} = 10^4 \times 10^4/4 = 2.5 \times 10^7$ features/cm^2. The practical detection limit is not limited by the beam divergence, since defect images sizes are typically greater than 1 μm. Threading dislocation images in GaN have a minimum feature size ≈ 10 μm, corresponding to the greatest achievable detection limit $N \approx (10 \times 10^4)^2 = 10^6$ dislocations cm^{-2}.

The recorded intensity distribution, also called a topograph, is proportional to the spatial distribution of the crystal's scattering power. A local change in scattering power due to, e.g. a crystal defect, is seen as contrast change in the recorded topograph. In the case of monochromatic radiation, only one set of lattice planes can fulfil Bragg's condition for diffraction, producing a single topograph, whereas polychromatic radiation fulfils Bragg's condition for diffraction for several sets of lattice planes simultaneously, resulting in several topographs.

X-ray diffraction spots recorded with monochromatic radiation were observed to have non uniform contrast already in 1931 by Berg [86], and the term topograph was first used by Ramachandran in 1944 [87]. The continuous part of the laboratory x-ray tube spectrum was used by Guinier and Tennevin in 1949 [88] to record white beam x-ray topographs, as reported in [89]. The x-ray tube radiation has low intensity and is weakly collimated, and it was the advent of the synchrotron that enabled fast and detailed studies of defects in crystalline ma-

terials. Early synchrotron radiation x-ray topography experiments of defects in Si were reported by Tuomi *et al.* in 1974 [89]. The field of synchrotron x-ray topography developed rapidly to aid crystal growers achieve higher quality crystals [90–92]

Topographs can be recorded in either back reflection geometry (Bragg case) or transmission geometry (Laue case). The back reflection measurement geometry is illustrated in figure 4.3. In back reflection topography the x-ray film is positioned between the light source and the sample. The incident x-rays (depicted blue in figure 4.3) traverse the hole in the x-ray film and are scattered backwards (depicted green in figure 4.3) onto the film by the sample. Due to the continuous wavelength distribution of synchrotron radiation, several sets of lattice planes simultaneously satisfy the Bragg condition for diffraction, equation (3.2), and several images of the defect structure are recorded at a single exposure. The sample is usually tilted slightly with respect to the incident beam to allow diffraction to be recorded from symmetric planes parallel to the sample surface.

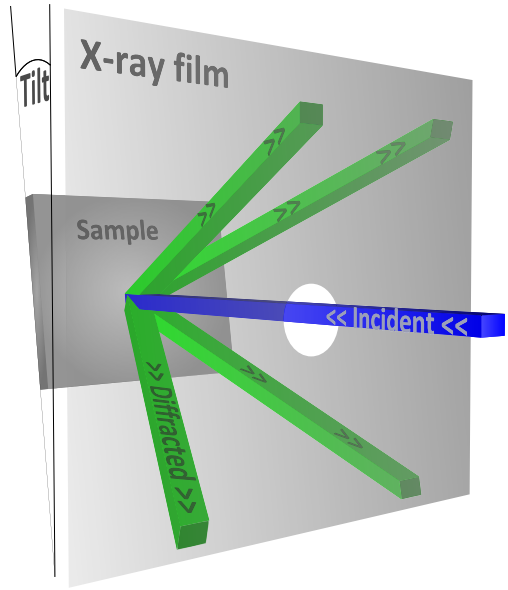

Figure 4.3. Back reflection x-ray topography. The incident beam is simultaneously diffracted backwards by several diffraction planes due to the continuous wavelength distribution. Each back reflected beam images the defect structure of the irradiated volume.

Back reflection is a convenient way to study the defect structure near the surface and the knowledge of measurement depth is therefore important. The measurement depth of back reflection topography can be estimated from x-ray

absorption with the Beer-Lambert law

$$I = I_0 e^{-\mu t}, \tag{4.3}$$

where I is the intensity after initial intensity I_0 has attenuated over a path length t. The linear absorption coefficient is wavelength dependent, i.e. $\mu = \mu(\lambda)$, and should be determined for each wavelength and therefore each topograph separately. The attenuation length is defined as the depth at which the intensity has fallen to 1/e and is according to equation (4.3) $1/\mu$. The attenuation length additionally depends on the sample tilt and the angle between the sample surface and diffracting planes, since the effective path length t_{eff} of x-rays at a perpendicular depth $t_\perp$ is $t_{\text{eff}} = t_\perp(\sin^{-1}(\beta_1)+\sin^{-1}(\beta_2))$, where β_1 and β_2 are the incident and exit beam angles. As an example, the perpendicular attenuation lengths of the 0008 topograph with λ = 1.2840 Å and the $02\bar{2}11$ topograph with λ = 0.8762 Å, discussed in publications I and II, are 9 μm and 27 μm, respectively. The values of μ were obtained from [93] and $\beta_1 = 82.5°$ is common for both reflections. The values of β_2 were $\beta_2 = \beta_1$ for the symmetric 0008 reflection and $\beta_2 = 71.7°$ for the asymmetric $02\bar{2}11$ reflection. Back reflection measurements were used in publications I, II, III and IV to identify dislocations and study grain boundaries.

Transmission x-ray topography records images formed by the transmitted, forward scattered x-rays. It is a complimentary technique to the back reflection geometry, since the two geometries probe different lattice planes. Additionally, back reflected x-rays provide information on the surface region, whereas transmitted x-rays probe the bulk of the crystal. In normal conditions the back reflection measurement records images from lattice planes angled at ≈ 20°-0° to the surface whereas the transmission geometry allows study of lattice planes angled at ≈ 70°-90° to the sample surface. Pure threading edge and pure threading screw dislocations (see section 2.3) can therefore be differentiated by combining the two measurement geometries.

A drawback of transmission SR-XRT is that the image is formed from a greater depth and the images of the dislocations may overlap. This geometry is therefore less suited for materials with dislocation density close to the detection limit. The section transmission measurement, a variant of the transmission geometry is schematically presented in figure 4.4. In section transmission measurements the vertical dimension of the incident beam, shown in blue, is reduced with a slit to ≈ 15 μm and the narrow beam irradiates a small section of the sample, thus reducing dislocation image overlap. Each forward diffracted beam, shown green in figure 4.4, provides a cross sectional image of the defect structure. This geometry was used in publications V and VI to evaluate the

quality of GaN grown by metallo organic vapour phase epitaxy on patterned substrates.

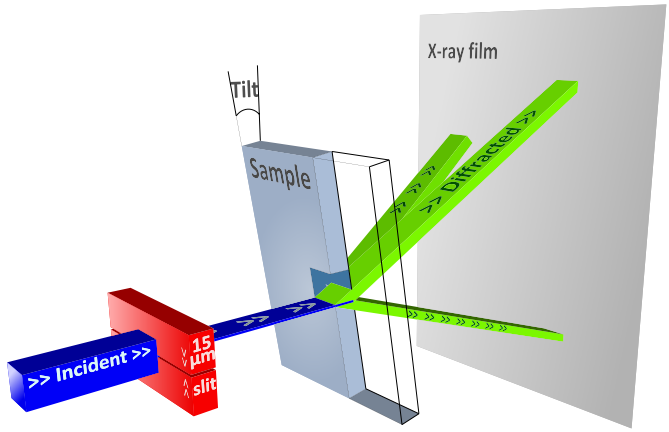

Figure 4.4. Section transmission x-ray topography. The incident beam height is limited by a slit to ≈ 15 μm. The vertically narrow beam is diffracted from both sides of the crystal and forms an image of the crystal cross section upon projection onto the x-ray film. Each forward diffracted beam images the defect structure of the irradiated volume.

The recorded diffraction pattern, or Laue pattern, is characteristic to each crystal structure. An example of a GaN Laue pattern recorded in transmission geometry is shown in figure 4.5. The topographs may be indexed by geometrical means with knowledge of the crystal structure, sample tilt angle and distance from sample to film. Simulated positions of the highest intensity topographs in figure 4.5 are shown in red, and some of the corresponding Miller indices in blue. The indexing software LauePt 3.0 [94] was used to index figure 4.5 and topographs in publications I, II and III. The software Orient Express 3.3 [95] was used to index topographs in publications V and VI. Several wavelengths may contribute to a single topograph, and the indexing software takes into account both the structure factor and the available wavelength distribution in determining the indices and dominant wavelengths of each topograph.

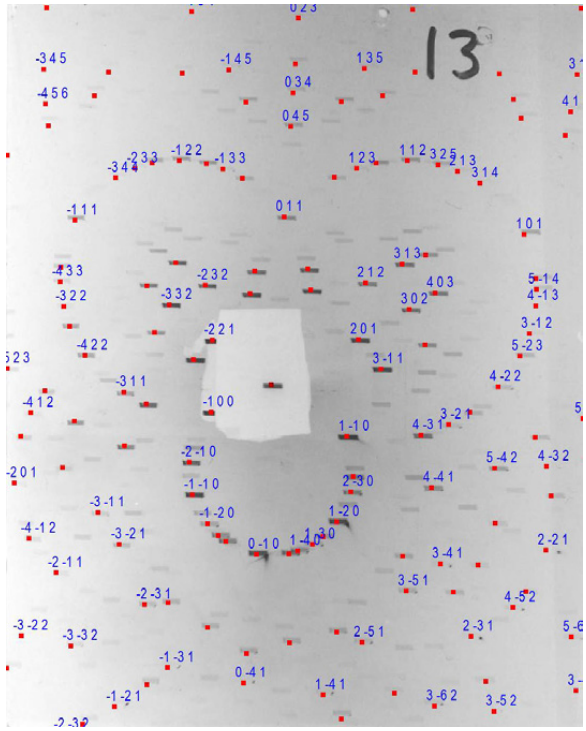

Figure 4.5. Transmission synchrotron radiation x-ray topography Laue pattern of GaN. The simulated positions of topographs with highest intensities are shown as red overlays and some of the corresponding Miller indices are shown as blue overlays. The topograph was recorded in HASYLAB in December 2011 and indexed with the software LauePt 3.0 [94].

4.3 Dislocation Visibility and Grain Boundaries

The amount of distortion a dislocation exerts on a given set of crystallographic planes depends on the dislocation's Burgers vector. Since a dislocation essentially shifts the surrounding lattice by a lattice vector or multiple thereof, some lattice planes remain undistorted. The invisibility criteria [96]

$$\begin{aligned} \mathbf{g}\cdot\mathbf{b} &= 0 \quad \text{for screw dislocations} \\ \mathbf{g}\cdot\mathbf{b} = 0 \text{ and } \mathbf{g}\cdot\mathbf{b}\times\mathbf{l} &= 0 \quad \text{for edge dislocations} \end{aligned} \tag{4.4}$$

state that screw dislocations are invisible whenever diffraction occurs from planes parallel to the Burgers vector, i.e. when the diffraction vector $\mathbf{g}$ is perpendicular to $\mathbf{b}$. Edge dislocations on the other hand are invisible when the cross product of the line vector and Burgers vector is perpendicular to the diffraction vector. Threading edge dislocations are therefore invisible in symmetric (000l) diffraction and threading screw dislocations in asymmetric (hki0) diffraction. Since the mixed dislocation is a combination of edge and screw dislocations, it must fulfil the invisibility criteria for both dislocation types, which

according to equation (4.4) are identical to the invisibility criteria for the edge dislocation. The invisibility criteria were used in publications I and III to distinguish between threading mixed and threading edge dislocations.

In crystalline materials, grains are uniform regions of single crystalline material separated by grain boundaries [35]. By definition, grains that share a grain boundary are differently oriented with respect to each other. Tilt is used to describe lattice rotation about an axis in the sample surface plane and twist to describe lattice rotation about the sample surface normal. Grain boundaries commonly accommodate a large number of dislocations. Lattice tilt in c-plane GaN is influenced mostly by threading screw dislocations, and lattice twist by threading edge dislocations and are direct consequences of equation (4.4). The misorientation of grains is seen in white beam topography measurements as displacement of diffraction images and was studied in publication III.

It is energetically favourable for dislocations with equal Burgers vectors to align in arrays and these are often observed at grain boundaries [35, 97]. The rotation α in radians of a grain boundary can be estimated by equation (4.5):

$$\sin\frac{\alpha}{2} = \frac{b}{2D} \Longrightarrow \alpha \approx \frac{b}{D},\ \alpha \ll 1 \tag{4.5}$$

where b is the Burgers vector length and D the spacing of the dislocations. The tilt caused by threading mixed dislocation arrays in GaN was estimated in publication II using equation (4.5).

4.4 Contrast in Synchrotron Radiation X-Ray Topography

A perfect crystal has no structural variation and therefore diffracts spatially homogeneously, resulting in a uniform topograph free of contrast variation. Defects however, introduce structural variation which is seen as contrast change in the topograph image. Several contrast mechanisms contribute to the SR-XRT image and they are commonly divided into two categories; orientation contrast and extinction contrast. The extinction contrast is further divided into the direct image contrast, dynamical image contrast and the intermediate contrast [98].

4.4.1 Extinction Contrast

The direct image contrast, also called the kinematical image contrast is the most commonly observed contrast type in dislocation images. It is observed when the angular or wavelength acceptance of the crystal is smaller than those

of the x-ray beam [84]. When this is true, x-rays incident on a perfect crystal are not fully diffracted and a large portion of the radiation is absorbed or transmitted without scattering [84]. The situation is different in the presence of a dislocation; the distorted region near a dislocation diffracts several wavelengths when irradiated with a polychromatic beam, resulting in an increase of diffracted x-ray intensity. The increased intensity around a dislocation is observed as darker contrast on a lighter background provided by the surrounding undistorted region. The intensity will increase with increasing degree of crystal mosaicity, until the crystal is ideally imperfect, i.e. the extinction approaches zero [99]. Direct image contrast is dominant in low absorption conditions when $\mu t < 1$, where μ is the wavelength dependent linear absorption coefficient and t the travelled distance of the x-rays inside the crystal. In back reflection topographs, μt is practically always less than unity and the back reflection images are dominated by direct image contrast. Direct image contrast was observed in publications I, II, III, V, IV and VI.

Dynamical image contrast is observed in high absorption conditions, i.e. when $\mu t > 6$. The dynamical theory of diffraction, which takes into account interference effects between diffracted and incident wave fields is needed in the interpretation of dynamical image contrast [90]. This contrast type is only observed in diffraction from near perfect crystals as even a small amount of lattice imperfection will obscure the interference effects. The best known dynamical image contrast are Pendellösung fringes commonly observed in high quality silicon section transmission topographs [100]. Dynamical image contrast was not observed in section transmission topographs in publications IV, V and VI due to too low structural quality.

The dislocation image is formed partially by direct image contrast and partially by dynamical image contrast in medium absorption conditions, when $1 < \mu t > 6$. This type of contrast is called intermediate contrast.

4.4.2 Orientation Contrast

Orientation contrast is caused by inhomogeneous diffraction of x-rays by misaligned parts of a crystal, such as grain boundaries, twin regions [92] or tilted epitaxial layers [101, 102]. Since grains are tilted and/or twisted with respect to each other, grain boundaries irradiated with a polychromatic beam are spatially displaced on the x-ray film. In SR-XRT the images from differently oriented crystal regions either overlap or are separated, depending on the type of misorientation [103]. Overlapping images appear darker due to locally increased x-ray intensity on the film, whereas separated regions appear lighter.

Orientation contrast was observed from grain boundaries in publication III.

Orientation contrast is also observed in images from smaller defects such as super screw dislocations and elemental screw dislocations. Simulations based on geometric distortion of the lattice surrounding screw dislocations and super screw dislocations in SiC, have shown that the topograph images of these defects are primarily formed by orientation contrast, instead of the direct image contrast [90]. Topograph images from threading screw dislocation in GaN are also dominated by orientation contrast, as shown in publication I.

4.5 Simulation of Screw Dislocation Contrast in Topography Images

White circular features similar to images from micropipes and super screw dislocations in SiC back reflection topographs [104, 105] were observed in publication IV. The screw dislocation 0008 back reflection topography contrast was simulated in publication I to determine the origin of these white defects. The images were simulated using an adaptation of the ray tracing approach, previously successful in simulation of micropipes and super screw dislocations in SiC [106]. In this model, the displacement field $\mathbf{u}$ of a threading screw dislocation was used to compute the deviation of the diffracting plane normal around a TSD from the normal of the undisturbed lattice.

The displacement field $\mathbf{u}$ of a threading screw dislocation propagating in the $\hat{\mathbf{z}}$-direction is [107]

$$\mathbf{u} = \frac{b}{2\pi} \arctan(\frac{y}{x})\, \hat{\mathbf{z}} \tag{4.6}$$

where x and y are the in-plane coordinates, b is the magnitude of the Burgers vector $\mathbf{b}$ and $\hat{\mathbf{z}}$ the unit vector. The equation for the deviated diffracting plane normal is [108]

$$\mathbf{n} = \mathbf{n_0} - \nabla(\mathbf{n_0} \cdot \mathbf{u}) \tag{4.7}$$

where $\mathbf{n_0}$ is the undisturbed normal. The sample surface was divided into a two dimensional grid and the diffracting plane normals were calculated for each grid element using equations (4.6) and (4.7). The diffraction normals were then used to geometrically simulate diffraction from a region near a threading screw dislocation. The diffracting elements were assumed identical and therefore the effects of x-ray penetration depth into the sample were omitted. The diffracted x-rays were then collected onto another two dimensional grid representing the x-ray film and the intensity distribution was finally plotted on a logarithmic scale to account for the logarithmic film response. The grid spa-

cings were 20 nm×20 nm for the sample and 200 nm×200 nm for the x-ray photographic film. The images of groups of closely spaced TSDs were simulated by adding the displacement fields of single dislocations prior to calculating the diffraction normals.

5. Defect Selective Etching of Gallium Nitride

Defect selective etching (DSE) is a well established defect characterization technique, in which a crystal is exposed to an etchant and defects are revealed as a result of different etch rate around defects [109]. Due to fluctuations in composition and/or physical structure, a suitable etchant etches the region around the defect faster or slower, resulting in etch pits or hillocks [109]. The etching method affects the etch pit shape. Etch pits in GaN have a whisker-like shape when etched by photoelectrochemical (PEC) etching, and regular hexagonal pits when etched by wet etching in, e.g. hot H_3PO_4 or KOH [110]. Wet etching has been reported to be more suitable for low defect density bulk GaN and it will hereafter be the only discussed method [111].

Different types of threading dislocations in GaN have been shown to etch at different rates and calibration with other defect characterization techniques, such as transmission electron microscopy and atomic force microscopy has enabled identification of threading edge, screw and mixed dislocations based on their etch pit sizes [112]. The inclination of the etch pit side wall has also been reported to be steeper for screw dislocations than edge dislocation, and can also be used as an indicator of dislocation type [112–115].

The common consensus is that the edge dislocation produces the smallest, mixed dislocation the intermediate and screw dislocation the largest size etch pit. This is in contradiction with expected size distribution based on Burgers vector magnitudes. The edge dislocation has the smallest Burgers vector magnitude $b = a$ and is therefore expected to etch slowest, producing the smallest etch pit, as observed. The mixed dislocation however, has the largest Burgers vector magnitude $b = a + c$ and should therefore have a larger etch pit than the screw dislocation with $b = c$. The screw dislocation etch pit is consistently reported larger, both in heteroepitaxial GaN and homoepitaxial GaN [115]. The discrepancy has been explained by a different impurity incorporation between the two defect types [115].

The choice of etchant and etching temperature affects the DSE results significantly; etching in low energy conditions may not reveal all dislocation types [109]. The etching time is also important as a too short time may not reveal all dislocations but a too long time will cause merging of etch pits, and consequently under estimation of defect density. DSE experiments in eutectic 450 °C KOH-NaOH for 30 minutes were utilized in publication I to reveal all types of defects. The etching experiments in publication I confirmed that most defects that appear as super screw dislocations in the topograph images are a result of adjacent threading dislocations with combined strain fields.

6. Analysis of Crystal Structure and Dislocations in GaN by SR-XRT

6.1 Threading Screw Dislocations in GaN Topograph Images

Figure 6.1 (a) shows a region of a 0008 back reflection topograph with two types of defects visible; large white defects with circular and curved irregular shapes, and smaller defects with black and white half moon-like contrast. The white features result from threading screw dislocations and groups of threading dislocations, as confirmed by the threading screw dislocation simulation in figure 6.1 (b). According to equation (4.6), the displacement field of a TSD or TSD group is directly proportional to the Burgers vector and can only have discrete values corresponding to net Burgers vector magnitudes $b = nc$, where n is an integer and c the out of plane lattice constant. Only discrete size white features were found even on a much greater scale, further supporting the conclusion the white defects are TSDs. The net Burgers vector values $|\mathbf{b}| \in [c, 3c]$ of each white feature lobe are annotated in figure 6.1 (b). Whether a TSD is left or right handed can not be determined for a single TSD from a symmetric topograph, but the handedness influences the appearance of TSD clusters, allowing determination of TSD net Burgers vector direction.

Based on the gained knowledge of the TSD topograph appearance in publication I, threading screw dislocations were successfully identified in publication III. A large area (5×1 mm^2) characterization of screw dislocation distribution in ammonothermal GaN was reported in publication II.

The back reflection topograph images do not reveal whether a $b = nc$ screw dislocation image is caused by adjacent dislocations with superposed strain fields or by true super screw dislocations. An example of this is shown in figure 6.2 where a $6c$ TSD image has been simulated as a single $6c$ dislocation in figure 6.2 (b), and as a single $1c$ dislocation surrounded by five $1c$ dislocations in pentagons with 2 μm and 3 μm radii, shown in figures 6.2 (c) 6.2 (d),

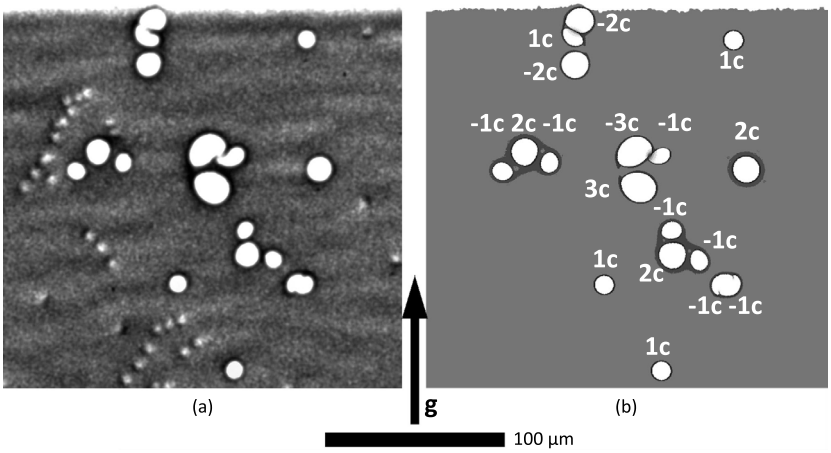

Figure 6.1. 0008 back reflection (a) and simulated (b) images of individual screw dislocations and screw dislocation clusters. The signs and magnitudes of the net Burgers vectors are marked on the simulated image. Image from publication I.

respectively.

Defect selective etch pit experiments were performed to study the fine structure of defects with net Burgers vectors $b > c$. Figure 6.3 clearly shows the topograph image of the $2c$ strain field in 6.3 (a) corresponds to two separate screw dislocation etch pits in figure 6.3 (b). All but one of the observed similar cases were reduced to single screw dislocations in close proximity. The one occurrence of a single etch pit and a $2c$ strain field topograph image could be the result of a super screw dislocation, but has not been confirmed by other means.

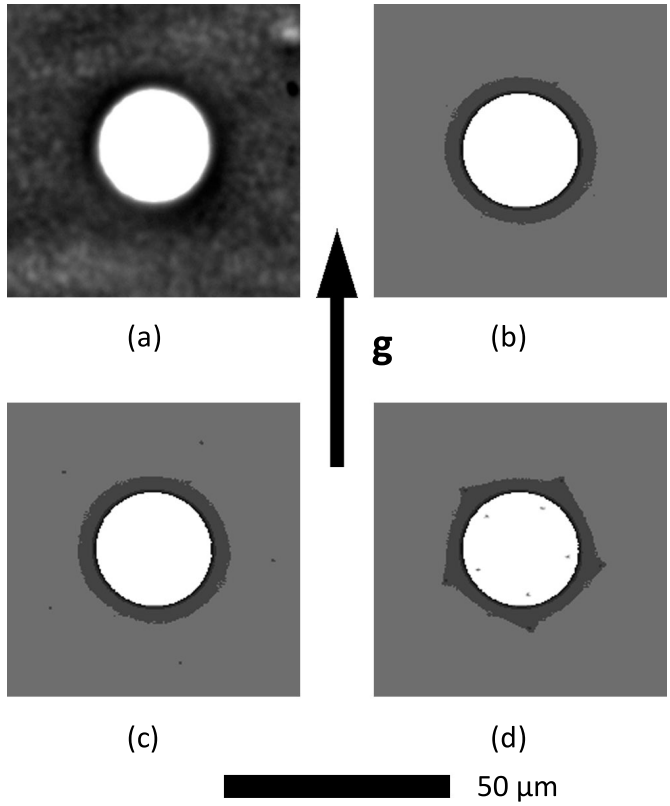

Figure 6.2. Experimental (a) and simulated (b)-(d) images of a defect with white area diameter corresponding to a 6*c* net Burgers vector. (b) was simulated assuming a 6*c* dislocation, (c) and (d) assuming six separate 1*c* dislocations arranged as a single dislocation surrounded by five dislocations in regular pentagons with 2 µm and 3 µm radii, respectively. The circular symmetry fails in (d), indicating the threshold distance when the bundle is distinguished from an individual dislocation. Image from publication I.

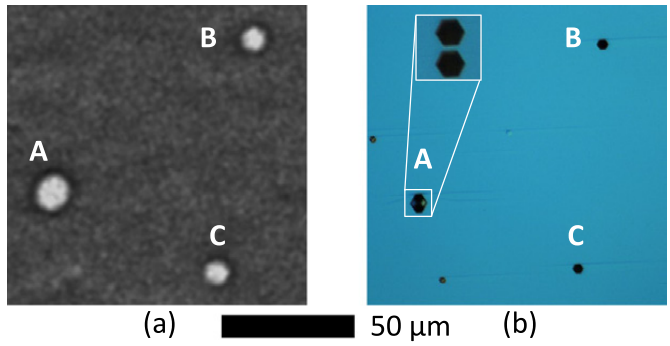

Figure 6.3. Comparison of a 0008 topograph (a) and a DSE image (b). The topograph image of a 2**c** strain field, dislocation A, corresponds to two etch pits with identical dimensions to dislocations B and C. The inset in (b) shows a magnification of the two less etched pits before merging. Image from publication I.

6.2 Threading Mixed Dislocation Contrast

Threading mixed dislocation contrast in GaN topographs was also determined in publication I. Figure 6.4 shows threading mixed dislocations in symmetric 0008, figure 6.4 (a), and asymmetric $02\bar{2}11$ topographs, figure 6.4 (b). Six distinct directions of black to white contrast were observed and these have been labelled with numbers 1-6 in figure 6.4. Examples of each type are shown enlarged in the bottom part of figure 6.4. The contrast direction was discussed in publication I and attributed to the different line directions of the mixed dislocation. The mixed dislocation has a line direction inclined away from the [0001] direction towards its Burgers vector [116, 117], and since the mixed dislocation edge component has six possible Burgers vectors, it must have six distinct contrast directions. The relation between edge component direction and black to white contrast direction of TMDs was utilized in publication II to estimate the effect of TMD arrays with identical Burgers vectors on lattice tilt and twist.

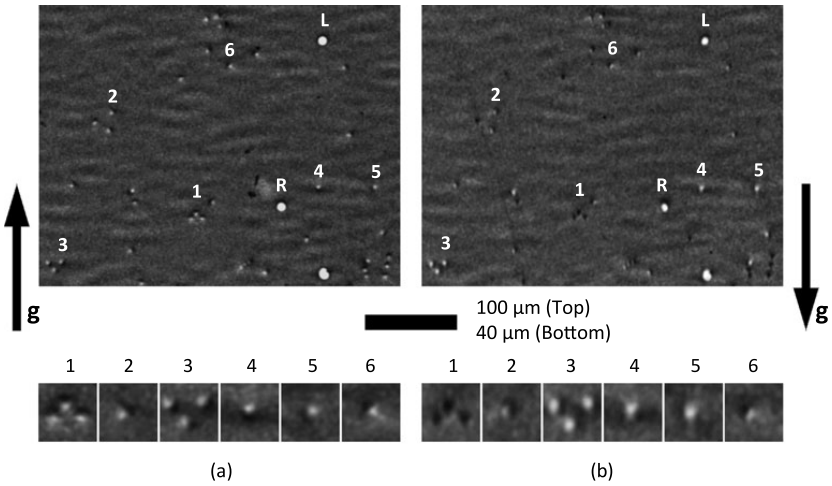

Figure 6.4. Symmetric 0008 (a) and asymmetric $02\bar{2}11$ (b) topographs of mixed dislocations. Examples of six distinct black to white contrast directions are labelled with numbers 1 to 6, and enlargements of each example are shown in the bottom of the image. Two elemental screw dislocations marked L and R have opposite slant in the $02\bar{2}11$ topograph due to opposite handedness. Image from publication I.

According to previous discussion, neighbouring threading mixed dislocations with equal direction screw components should produce a $2c$ 0008 topograph image, since the Burgers vectors are summed and the net Burgers vector affecting the symmetric topograph is $b = 2c$. An example of this is shown in figure 6.5, where two $2c$ topograph images in figure 6.5 (a) are reduced to two mixed dislocation etch pit pairs in the defect selective etching image in figure 6.5 (b).

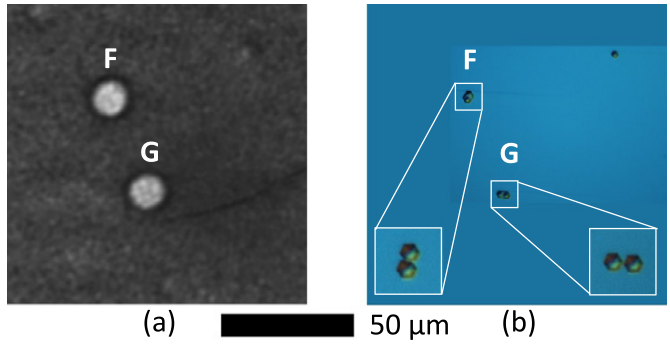

Figure 6.5. Comparison of a 0008 topograph (a) and a DSE image (b). Both images of 2**c** strain fields, marked F and G, are represented by pairs of mixed dislocations in close proximity. The insets in (b) were recorded after shorter etching time and display the etch pits clearly separated. Image from publication I.

6.3 Dislocation Arrays

Publication II discusses threading dislocation distribution over a large area and reported on dislocation clustering in the form of mixed dislocation arrays. Figure 6.6 shows a part of a 0008 topograph, were three threading mixed dislocation arrays have been marked and labelled A, B and C. Each array consists of threading mixed dislocations with equal black to white contrast directions and therefore equal Burgers vectors. The average distances between dislocations inside the arrays were determined for each stripe, and lattice tilt and twist were estimated using the distance values with equation (4.5).

The tilt and twist values estimated with equation (4.5) are too small (≤ 10 arc seconds) to yield observable orientation contrast and HRXRD ω rocking curves were recorded around symmetric (0002) and asymmetric ($20\bar{2}1$) planes to determine the extent of lattice misorientation caused by the dislocation arrays. The ω rocking curves recorded with decreasing x-ray beam sizes are shown in figure 6.7, where it is clearly seen that the number of diffraction maxima in the symmetric (0002) rocking curve decreases with decreasing x-ray beam size. The asymmetric ($20\bar{2}1$) displays a high intensity peak and a low intensity shoulder in all rocking curves. The lattice tilt and twist values were determined based on the angular separation of rocking curve maxima. The values agreed within a few arc seconds with the values estimated from dislocation spacing.

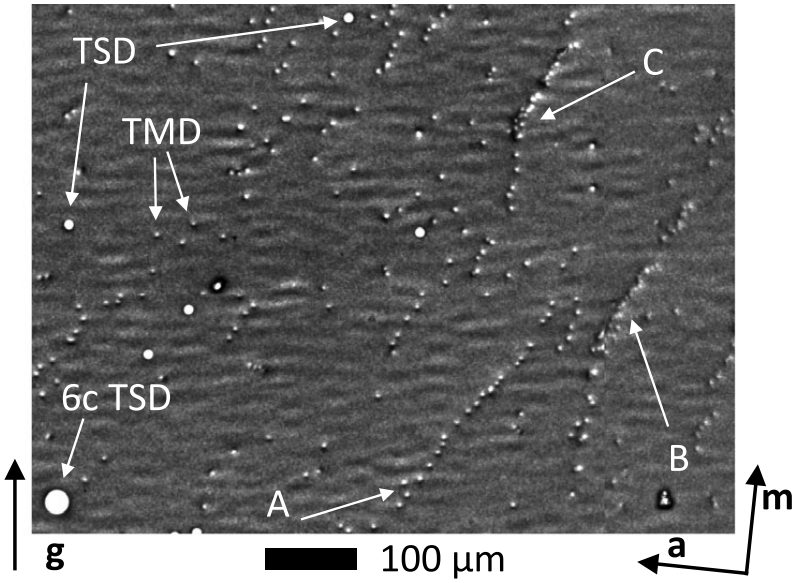

Figure 6.6. Part of a 0008 back reflection topograph. Examples of threading screw dislocations (TSD) and threading mixed dislocations (TMD) have been marked with arrows. Three TMD arrays have been marked A, B and C and an image corresponding to a strain field with a net Burgers vector 6c has been labelled 6c TSD. Image from publication II.

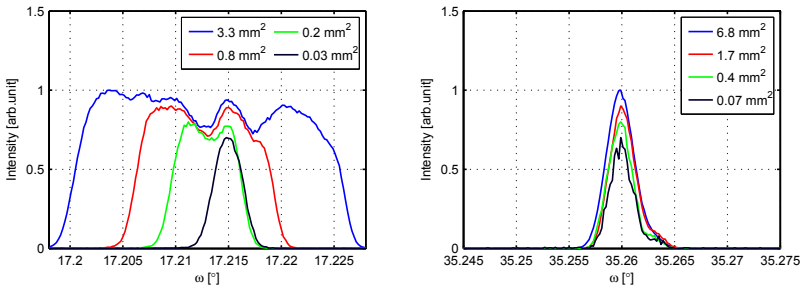

(a) (b)

Figure 6.7. XRD ω rocking curves around (0002) (a) and $(20\bar{2}1)$ (b) reflections for different x-ray beam sizes. The number of diffraction maxima observed in (a) decreases with decreasing beam size, while the number of maxima is constant in (b). Image from publication II.

6.4 Grain Boundaries

The SR-XRT images of grain boundaries were discussed in publication III. Figure 6.8 shows 0008, $10\bar{1}7$ and $\bar{1}017$ topograph images of three grain boundaries marked GB 1, GB 2 and GB 3. The orientation contrast is clearly visible in figure 6.8, where the grain boundaries display either white or dark contrast corresponding to overlapping and separated x-rays. Since lattice tilt affects only symmetric crystallographic planes, the GB 1 separation in figure 6.8(b) with **g** = [0008] is caused by pure tilt. The size of GB 1 does not change dramatically in figures 6.8(a) and 6.8(c), indicating the lattice twist is small. The opposite is true for grain boundaries GB 2 and GB 3. These grain boundary images overlap slightly in the symmetric 0008 topograph in figure 6.8(b), but show larger separation and overlap in asymmetric topographs, in figures 6.8(c) and 6.8(a). This indicates significant lattice twist but small lattice tilt. The grain boundaries GB 2 and GB 3 display opposite contrast in the asymmetric topographs and have therefore opposite sign twist values. The tilt and twist values of grain boundaries GB 1- GB 3 were determined from 0008, $10\bar{1}8$ and $\bar{1}018$ topographs recorded at three different distances in publication III. The tilt and twist values agreed well with XRD rocking curve measurements, also discussed in publication III.

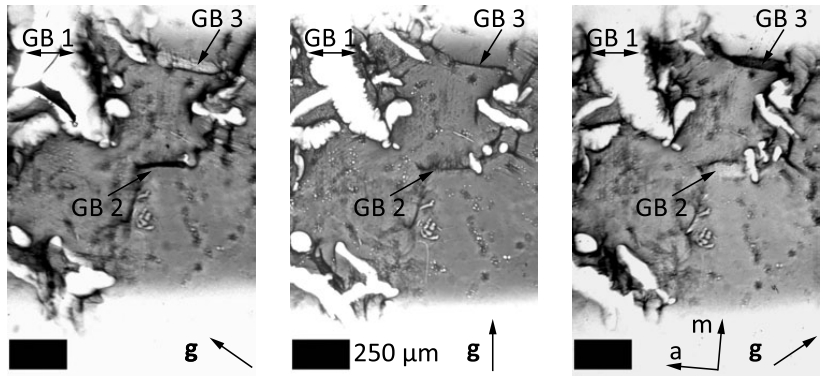

(a) (b) (c)

Figure 6.8. Back reflection topographs of grain boundaries GB 1-GB 3 with diffraction vectors (a) $10\bar{1}7$, (b) 0008 and (c) $\bar{1}017$ and dominant λ = 1.3676, 1.2824, 1.3667 Å. Images were recorded at sample-to-film distance 40 mm. Grain boundary size and brightness depend on the diffraction vector and sample to film distance and were used to estimate grain boundary tilt and twist. Image from publication III.

6.5 Basal Plane Dislocations

Dislocations with significant in-plane line direction components were observed in publication III. These are likely to be basal plane dislocations and appear as lines rather than points due to the back reflection measurement geometry. Most of the lines were observed in conjunction with grain boundaries. Figure 6.9 displays a grain boundary with vertical dark lines parallel to $[01\bar{1}0]$ visible in figure 6.9(b), but invisible in figures 6.9(a) and 6.9(c). The Burgers vector (projection) was determined by the invisibility criterion, equation (4.4), and was found to be $\pm\frac{1}{3}[\bar{1}2\bar{1}0]$. Similar dislocation line images were also observed in directions rotated approximately 60° to each other. The basal plane dislocation line directions $\langle 1\bar{1}00\rangle$ observed in publication III are less common than the line directions $1/3\langle 11\bar{2}0\rangle$ [118]. Misfit dislocations with equal line directions have been observed before in semipolar [119] and polar [120] heteroepitaxy, and the source of the dislocations have been speculated to be pre-existing dislocations [121]. The dislocations in figure 6.9 could therefore be misfit dislocations, created during growth by lattice mismatch between the seed crystal and the epilayer.

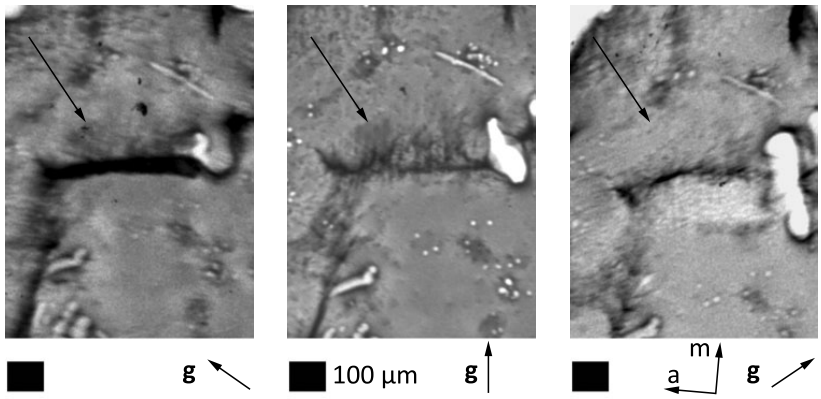

Figure 6.9. Back reflection topographs of grain boundary GB 2 with diffraction vectors (a) $10\bar{1}7$, (b) 0008 and (c) $\bar{1}017$ and dominant λ = 1.3676, 1.2824, 1.3667 Å. Images were recorded at sample-to-film distance 40 mm. The dark approximately upright dislocation lines marked with arrows are visible in (b) but not in (a) and (c) and have therefore a Burgers vector parallel to $[\bar{1}2\bar{1}0]$. Image from publication III.

6.6 Strain distribution

Symmetric (0002) and asymmetric (11$\bar{2}$4) reciprocal space maps were used in publication III to study strain distribution and overall crystal quality. The RSMs are shown in figure 6.10(a), where it is seen that the asymmetric (11$\bar{2}$4) reciprocal lattice point is noticeably broader than the symmetric (0002) reciprocal lattice point. This indicates greater lattice twist than lattice tilt, most probably caused by a high density of basal plane dislocations and threading edge dislocations at grain boundaries.

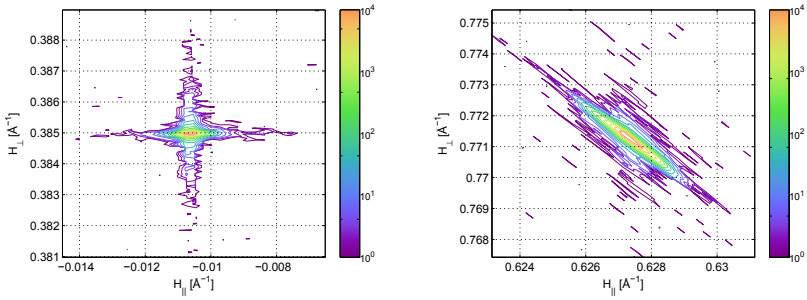

(a) (b)

Figure 6.10. (a) Symmetric (0002) and (b) asymmetric (11$\bar{2}$4) reciprocal space maps. Images are scaled identically for easy comparison. Image from publication III.

The FWHM and maximum values of the RSMs were used to calculate the strain distribution using equation (3.3). Normally, strain is calculated using the lattice constants of the sample and a reference value. In publication III however, the strain variation within the sample was estimated using the RSM maximum value as the reference value and the FWHM as the deviated value. The in plane and out of plane values were found to be $|\Delta\epsilon_a| = 0.0147$ % and $|\Delta\epsilon_c| = 0.0109$ %. These values show the strain variation is very small within the measurement depths of 10 μm and 6 μm for (0002) and (11$\bar{2}$4) reflections, respectively.

6.7 Epitaxial GaN

The crystal structures of GaN films grown by MOVPE on patterned substrates and ammonothermal GaN wafers were discussed in publications IV, V and VI. The homoepitaxial GaN layer in publication IV was found to be of excellent crystal quality. Figure 6.11 shows the ω rocking curves around the symmetric (0002) and asymmetric (12$\bar{3}$1) reflections. The FWHM of both reflections

were 9 arc seconds, a value at the very limit of the practical resolution of the XRD measurement equipment. The extremely narrow rocking curves show lack of substantial broadening due to threading dislocations, indicating the cystal quality of the homoepitaxial layer is comparable to that of the substrate.

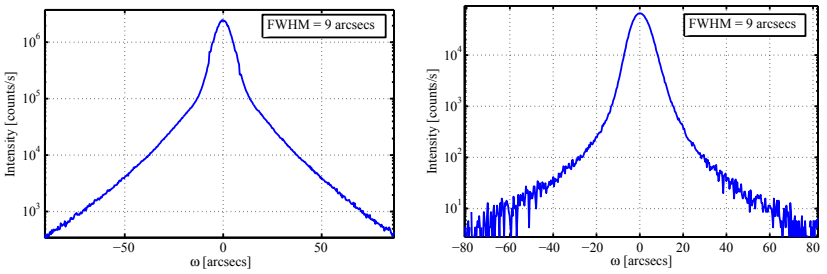

(a) (b)

Figure 6.11. ω rocking curves from homoepitaxial GaN around the (0002) (a) and the $(12\bar{3}1)$ reflections (b). The FWHM of both rocking curves were at the limit of the measurement setup resolution, ≈ 9 arc seconds. The small FWHM values indicate the homoepitaxial GaN layer is of excellent crystal quality. Image from publication IV.

The effect of patterning GaN/sapphire substrates on the overgrown epitaxial layer crystal quality was studied in publication V. In addition to a non-patterned reference sample, two patterned samples with different hole diameters were studied. Figure 6.12 displays the symmetric (002) and asymmetric (102) ω rocking curves from the reference sample (Sample R) and patterned samples with hole diameters 2 μm and 4.5 μm, samples A and B, respectively. As can be seen in figure 6.12, the asymmetric FWHM of sample B is notably narrower, while the symmetric FWHM is not. This indicates smaller lattice twist and a reduction in threading edge dislocation density due to the patterning of the substrate.

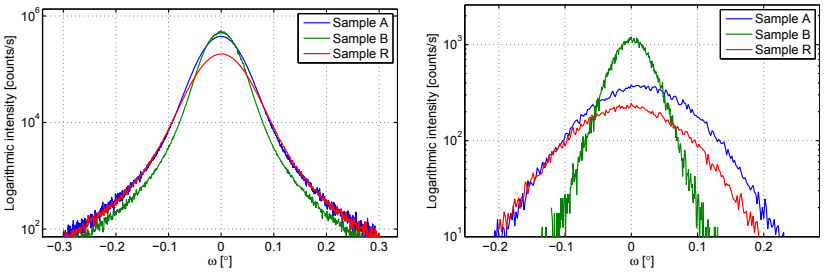

(a) (b)

Figure 6.12. ω rocking curves from homoepitaxial GaN around the (002) (a) and the (102) reflections (b). The (102) FWHM of sample B is smaller than the FWHM of the reference sample R by a factor of 2.6, indicating reduced lattice tilt in sample B. Image from publication V.

The samples in publication V were also studied by SR-XRT in transmission section geometry. An example of a section transmission topograph is given in figure 6.13, where the $\bar{1}20$ topograph of GaN and $\bar{1}10$ of sapphire from sample B are shown. The GaN epilayer image is dark, fuzzy and lacks structural detail, although it is the best quality sample studied in publication V. The section transmission geometry is better suited for thinner samples and/or samples with lower defect density.

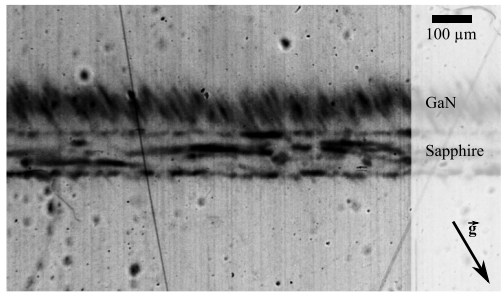

Figure 6.13. SR-XRT section transmission $\bar{1}20$ topograph of GaN and $\bar{1}10$ of sapphire from sample B. The fuzzy GaN epilayer image indicates poor crystal quality, and structural details cannot be resolved from the topograph. Image from publication V.

The (002) $2\theta - \omega$ scans of MOVPE grown GaN layers on patterned sapphire substrates are shown in figure 6.14. Figure 6.14 includes the $2\theta - \omega$ scans of epitaxial GaN on a non-patterned reference sample, GaN grown on a patterned sapphire substrate with a pillar structure (PS) and GaN grown on a sapphire substrate with hole structure (HS). The hole structure consisted of hexagonal holes with 2.5 μm hole diameter and 2.5 μm spacing, and the pillar structure was an inversion of the hole structure. As can be seen in figure 6.14, the (002) $2\theta - \omega$ maximum of the pillar structure is at a higher angle than the other maxima, indicating decreased strain and lattice constants closer to the strain free GaN.

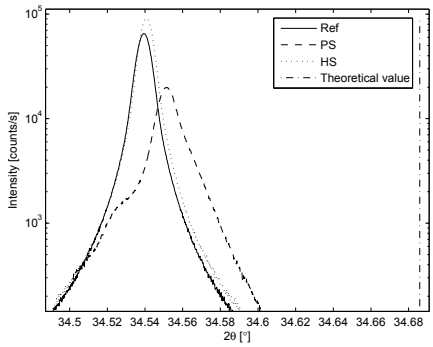

Figure 6.14. (002) $2\theta - \omega$ scans of GaN films on a non-patterned reference substrate, a pillar structure (PS) patterned sapphire substrate and a hole structure (HS) patterned sapphire substrate. The PS patterned sample has relaxed towards the theoretical value of strain free GaN. Image from publication VI.

7. Summary

The crystal structure and crystallographic defects in GaN were analysed by synchrotron radiation x-ray topography, x-ray diffraction and defect selective etching. The aim of this thesis was to non destructively reveal new knowledge on defects in free standing GaN, homoepitaxial GaN and heteroepitaxial GaN grown on patterned substrates.

SR-XRT was used to characterize dislocations and grain boundaries in bulk GaN grown by the ammonothermal method. The screw dislocation topograph image contrast was successfully simulated, and the appearances of threading mixed and threading screw dislocations in synchrotron topograph images were determined. This enabled identification of individual dislocations and discrimination between different types of dislocations. Large area characterization of defect structures of free standing GaN wafers were performed.

Images of defects with strain fields corresponding to dislocations with large screw components were observed in the free standing GaN wafers. Simulations indicate they are caused by strain fields corresponding to multiples of the elemental screw dislocation strain field. Defect selective etching experiments were performed to investigate whether the large dislocation images are caused by single dislocations, such as micropipes and super screw dislocations, or by the collective strain fields of groups of closely spaced elemental screw dislocations. The DSE measurements show that in all but one instance, the seemingly large dislocations are reduced to pairs or groups of elemental dislocations.

The large area study shows threading mixed dislocations are not randomly distributed, but exhibit signs of clustering. Threading mixed dislocations were observed to form arrays of dislocations with equal Burgers vectors. The dislocation arrays cause small lattice tilt and twist. The values of lattice tilt and twist were calculated based on the dislocation spacing and confirmed by high resolution x-ray diffraction measurements.

Epitaxial GaN layers grown by metallo organic vapour phase epitaxy were

also studied by SR-XRT and XRD. Heteropitaxial GaN layers were grown on patterned sapphire substrates and substrates consisting of patterned GaN layers grown on sapphire by MOVPE. Growth on patterned substrates was found to have a small impact on the defects density. Homoepitaxial layers were grown by MOVPE on ammonothermal GaN substrates and SR-XRT and XRD experiments show that the epilayer retains the substrate crystal quality.

The results of this thesis are important in understanding the defect structure of GaN, with emphasis on low defect density free standing substrates. The knowledge of the large area defect structure is vital for further structural improvement of GaN. The thesis established a basis for identifying and quantifying threading dislocations in GaN by SR-XRT, and future work should extend the large area analysis from a few mm^2 to cover the whole wafer area. Another topic of interest is the threading of dislocations into the epitaxially grown device layers. SR-XRT imaging of a whole wafer before and after epitaxy should allow to determine whether all dislocations thread to the device layer and if new dislocations are created during epitaxial growth. Finally, the impact of individual dislocations and dislocation clusters on device performances could be evaluated by combining SR-XRT and device performance characterization methods.

References

[1] S. NAKAMURA, T. MUKAI and M. SENOH. Candela class high brightness InGaN/AlGaN double heterostructure blue light emitting diodes. *Applied Physics Letters* **64**, 13 (1994), 1687–1689.

[2] H. AMANO. Progress and Prospect of the Growth of Wide-Band-Gap Group III Nitrides: Development of the Growth Method for Single-Crystal Bulk GaN. *Japanese Journal of Applied Physics* **52**, (2013), 050001.

[3] A. BERGH. Blue laser diode (LD) and light emitting diode (LED) applications. *Physica Status Solidi (a)* **201**, 12 (2004), 2740–2754.

[4] OSRAM GMBH. *Green light for laser projectors*. 18 Oct. 2012. URL: http://www.osram.com/osram_com/press/press-releases/_trade_press/2012/green-light-for-laser-projectors/index.jsp (visited on 22/07/2014).

[5] NICHIA CORP. *The new development of High-power Green Laser Diodes*. 22 Nov. 2012. URL: http://www.nichia.co.jp/en/about_nichia/2012/2012_112201.html (visited on 22/07/2014).

[6] BMW GROUP. *BMW Laser Light goes into series production. The BMW i8 is the first production vehicle to feature the innovative light technology*. 10 Feb. 2014. URL: https://www.press.bmwgroup.com/global/pressDetail.html?title=bmw-laser-light-goes-into-series-production-the-bmw-i8-is-the-first-production-vehicle-to-feature-the&outputChannelId=6&id=T0165849EN&left_menu_item=node__8610# (visited on 22/07/2014).

[7] OSRAM GMBH. *Osram is the System Partner for Laser Light in the BMW i8*. 21 Feb. 2014. URL: http://www.osram.com/osram_com/press/press-

releases/_trade_press/2014/osram-is-the-system-partner-for-laser-light-in-the-bmw-i8/index.jsp (visited on 22/07/2014).

[8] E. MATIOLI, C. NEUFELD, M. IZA, S. C. CRUZ, A. A. AL-HEJI, X. CHEN, R. M. FARRELL, S. KELLER, S. DENBAARS, U. MISHRA, S. NAKAMURA, J. SPECK and C. WEISBUCH. High internal and external quantum efficiency InGaN/GaN solar cells. *Applied Physics Letters* **98**, 2 (2011), 021102.

[9] L. F. EASTMAN and U. K. MISHRA. The toughest transistor yet [GaN transistors]. *Spectrum, IEEE* **39**, 5 (2002), 28–33.

[10] M. SU, C. CHEN and S. RAJAN. Prospects for the application of GaN power devices in hybrid electric vehicle drive systems. *Semiconductor Science and Technology* **28**, 7 (2013), 074012.

[11] U. MISHRA and L. SHEN. GaN-based RF power devices and amplifiers. *Proceedings of the IEEE* **96**, 2 (2008), 287–305.

[12] L. LIU and J. H. EDGAR. Substrates for gallium nitride epitaxy. *Materials Science and Engineering: R: Reports* **37**, 3 (2002), 61–127.

[13] J. SPECK and S. ROSNER. The role of threading dislocations in the physical properties of GaN and its alloys. *Physica B: Condensed Matter* **274**, (1999), 24–32.

[14] V. AVRUTIN, D. J. SILVERSMITH, Y. MORI, F. KAWAMURA, Y. KITAOKA and H. MORKOC. Growth of Bulk GaN and AlN:Progress and Challenges. *Proceedings of the IEEE* **98**, 7 (2010), 1302–1315.

[15] H. YAMANE and M. SHIMADA. Preparation of GaN single crystals using a Na flux. *Chemistry of Materials* **1896**, 1 (1997), 413–416.

[16] F. KAWAMURA, M. MORISHITA, M. TANPO, M. IMADE, M. YOSHIMURA, Y. KITAOKA, Y. MORI and T. SASAKI. Effect of carbon additive on increases in the growth rate of 2in GaN single crystals in the Na flux method. *Journal of Crystal Growth* **310**, 17 (2008), 3946–3949.

[17] M. BOĆKOWSKI, P. STRAK, I. GRZEGORY and S. POROWSKI. "High Pressure Solution Growth of Gallium Nitride". *Technology of Gallium Nitride Crystal Growth*. Ed. by D. EHRENTRAUT, E. MEISSNER and M. BOĆKOWSKI. Part 4, Springer, 2010. Chap. 10.

[18] M. LESZCZYNSKI, P. PRYSTAWKO, R. CZERNECKI, J. LEHNERT, T. SUSKI and P. PERLIN. III-N ternary epi-layers grown on the GaN bulk crystals. *Journal of Crystal Growth* **231**, (2001), 352–356.

[19] M. Leszczynski, H. Teisseyre, T. Suski, I. Grzegory, M. Bockowski, J. Jun, S. Porowski, K. Pakula, J. M. Baranowski, C. T. Foxon and T. S. Cheng. Lattice parameters of gallium nitride. *Applied Physics Letters* **69**, 1 (1996), 73.

[20] A. Usui and H. Sunakawa. Thick GaN epitaxial growth with low dislocation density by hydride vapor phase epitaxy. *Japanese Journal of Applied Physics* **899**, (1997).

[21] K. Fujito, S. Kubo, H. Nagaoka, T. Mochizuki, H. Namita and S. Nagao. Bulk GaN crystals grown by HVPE. *Journal of Crystal Growth* **311**, 10 (2009). Proceedings of the 2nd International Symposium on Growth of III Nitrides, 3011–3014.

[22] R. Dwiliński, R. Doradziński, J. Garczyński, L. Sierzputowski, A. Puchalski, Y. Kanbara, K. Yagi, H. Minakuchi and H. Hayashi. Excellent crystallinity of truly bulk ammonothermal GaN. *Journal of Crystal Growth* **310**, (2008), 3911–3916.

[23] T. Hashimoto, F. Wua, J. S. Speck and S. Nakamura. Ammonothermal growth of bulk GaN. *Journal of Crystal Growth* **310**, (2008), 3907–3910.

[24] S. Pimputkar, S. Kawabata, J. S. Speck and S. Nakamura. Surface morphology study of basic ammonothermal GaN grown on non-polar GaN seed crystals of varying surface orientations from m-plane to a-plane. *Journal of Crystal Growth* **368**, (2013), 67–71.

[25] D. Tomida, Y. Kagamitani, Q. Bao, K. Hazu, H. Sawayama, S. Chichibu, C. Yokoyama, T. Fukuda and T. Ishiguro. Enhanced growth rate for ammonothermal gallium nitride crystal growth using ammonium iodide mineralizer. *Journal of Crystal Growth* **353**, (2012), 59–62.

[26] T. Sochacki and M. Amilusik. Preparation of free-standing GaN substrates from GaN layers crystallized by hydride vapor phase epitaxy on ammonothermal GaN seeds. *Japanese Journal of Applied Physics* **53**, (2014), 1–6.

[27] T. Sochacki, Z. Bryan, M. Amilusik, M. Bobea, M. Fijalkowski, I. Bryan, B. Lucznik, R. Collazo, J. L. Weyher, R. Kucharski, I. Grzegory, M. Bockowski and Z. Sitar. HVPE-GaN grown on MOCVD-GaN/sapphire template and ammonothermal GaN seeds:

Comparison of structural, optical, and electrical properties. *Journal of Crystal Growth* **394**, (2014), 55–60.

[28] S. PIMPUTKAR. “Ammonothermal Growth of Gallium Nitride”. Ph.D. University of California Santa Barbara, 2012.

[29] A. D. HANSER and K. R. EVANS. “Development of the Bulk GaN Substrate Market”. *Technology of Gallium Nitride Crystal Growth*. Ed. by D. EHRENTRAUT, E. MEISSNER and M. BOĆKOWSKI. Part 1, Springer, 2010. Chap. 1.

[30] D. EHRENTRAUT and R. PAKALAPATI. High quality, low cost ammonothermal bulk GaN substrates. *Japanese Journal of Applied Physics* **52**, (2013), 1–4.

[31] R. DORADZIŃSKI, R. DWILIŃSKI, J. GARCZYŃSKI, L. SIERZPUTOWSKI and Y. KANBARA. “Ammonothermal Growth of GaN Under Ammono-Basic Conditions”. *Technology of Gallium Nitride Crystal Growth*. Ed. by D. EHRENTRAUT, E. MEISSNER and M. BOĆKOWSKI. Part 3, Springer, 2010. Chap. 7.

[32] B. D. CULLITY and S. R. STOCK. *Elements of X-ray Diffraction*. 3rd ed. New Jersey: Pearson, 2001.

[33] H. MORKOÇ. *Nitride semiconductor devices, fundamentals and applications*. Weinheim: Wiley-VCH, 2013.

[34] H. MASUI, S. NAKAMURA, S. P. DENBAARS and U. MISHRA. Nonpolar and semipolar III-nitride light-emitting diodes: achievements and challenges. *IEEE transactions on Electron Devices* **57**, 1 (2010), 88–100.

[35] D. HULL and D. BACON. *Introduction to dislocations*. 4th ed. Boston: Butterworth-Heinemann, 2001.

[36] A. COTTRELL. Theory of dislocations. *Progress in Metal Physics* **1**, (1949), 77–126.

[37] N. MOTT. The mechanical properties of metals. *Proceedings of the Physical Society. Section B* **729**, (1951).

[38] N. MOTT. Dislocations and the theory of solids. *Nature* **171**, (1953), 234–237.

[39] H. KLAPPER. “Generation and propagation of defects during crystal growth”. *Springer Handbook of Crystal Growth*. Springer, 2010, 93–132.

[40] M. F. ASHBY and D. R. H. JONES. “Dislocations and Yielding in Crystals”. *Engineering materials 1: an introduction to properties, applications and design*. Part 1, Elsevier, 2012. Chap. 9.

[41] M. SYVÄJÄRVI, R. YAKIMOVA and E. JANZÉN. Anisotropic etching of SiC. *Journal of The Electrochemical Society* **147**, 9 (2000), 3519–3522.

[42] Y. CHEN, G. DHANARAJ, M. DUDLEY, E. K. SANCHEZ and M. F. MACMILLAN. Sense determination of micropipes via grazing-incidence synchrotron white beam x-ray topography in 4H silicon carbide. *Applied Physics Letters* **91**, 7 (2007), 071917.

[43] M. DUDLEY, J. BAI, X. HUANG, W. VETTER, G. DHANARAJ and B. RAGHOTHAMACHAR. Synchrotron white beam X-ray topography, transmission electron microscopy and high-resolution X-ray diffraction studies of defects and strain relaxation processes in wide band gap semiconductor crystals and thin films. *Materials Science in Semiconductor Processing* **9**, 1-3 (2006), 315–322.

[44] Y. CHEN, M. DUDLEY, E. K. SANCHEZ and M. F. MACMILLAN. Simulation of Grazing-Incidence Synchrotron White Beam X-ray Topographic Images of Micropipes in 4H-SiC and Determination of Their Dislocation Senses. *Journal of Electronic Materials* **37**, 5 (2007), 713–720.

[45] W. VETTER and M. DUDLEY. Surface-relaxation contributions to axial screw dislocation contrast in synchrotron white-beam X-ray topographs of SiC. *Journal of Applied Crystallography* (2002), 689–695.

[46] W. M. VETTER and M. DUDLEY. Micropipes in Silicon Carbide Crystals: Do all Screw Dislocations have Open Cores? *Journal of Materials Research* **15**, (08 2000), 1649–1652.

[47] W. M. VETTER and M. DUDLEY. Micropipes and the closure of axial screw dislocation cores in silicon carbide crystals. *Journal of Applied Physics* **96**, 1 (2004), 348.

[48] A. E. ROMANOV, E. C. YOUNG, F. WU, A. TYAGI, C. S. GALLINAT, S. NAKAMURA, S. P. DENBAARS and J. S. SPECK. Basal plane misfit dislocations and stress relaxation in III-nitride semipolar heteroepitaxy. *Journal of Applied Physics* **109**, 10, 103522 (2011), pages.

[49] S. C. JAIN, A. H. HARKER and R. A. COWLEY. Misfit strain and misfit dislocations in lattice mismatched epitaxial layers and other systems. *Philosophical Magazine A* **75**, 6 (1997), 1461–1515.

[50] T. SEONG, J. HAN, H. AMANO and H. MORKOC. *III-Nitride based light emitting diodes and applications*. Vol. 126. New York: Springer, 2013.

[51] G. B. STRINGFELLOW. *Organometallic vapor-phase epitaxy: theory and practice*. Academic Press, 1999.

[52] P. GIBART. Metal organic vapour phase epitaxy of GaN and lateral overgrowth. *Reports on Progress in Physics* **67**, 5 (2004), 667.

[53] T. SWAN. Thomas Swan Scientific Equipment Ltd. (2004).

[54] H. AMANO, N. SAWAKI, I. AKASAKI and Y. TOYODA. Metalorganic vapor phase epitaxial growth of a high quality GaN film using an AlN buffer layer. *Applied Physics Letters* **48**, 5 (1986), 353–355.

[55] M. ALI, A. ROMANOV, S. SUIHKONEN, O. SVENSK, P. TÖRMÄ, M. SOPANEN, H. LIPSANEN, M. ODNOBLYUDOV and V. BOUGROV. Void shape control in GaN re-grown on hexagonally patterned mask-less GaN. *Journal of Crystal Growth* **315**, 1 (2011). 15th International Conference on Metalorganic Vapor Phase Epitaxy (ICMOVPE-XV), 188–191.

[56] M. ALI, A. ROMANOV, S. SUIHKONEN, O. SVENSK, S. SINTONEN, M. SOPANEN, H. LIPSANEN, V. NEVEDOMSKY, N. BERT, M. ODNOBLYUDOV and V. BOUGROV. Analysis of threading dislocations in void shape controlled GaN re-grown on hexagonally patterned mask-less GaN. *Journal of Crystal Growth* **344**, 1 (2012), 59–64.

[57] S. SUIHKONEN, M. ALI, O. SVENSK, S. SINTONEN, M. SOPANEN, H. LIPSANEN, P. T. TÖRMÄ, V. NEVEDOMSKY and N. BERT. Patterning of sapphire/GaN substrates. *Physica Status Solidi (c)* **8**, 5 (2011), 1509–1512.

[58] R. DWILIŃSKI, R. DORADZIŃSKI, J. GARCZYŃSKI, L. SIERZPUTOWSKI, A. PUCHALSKI, Y. KANBARA, K. YAGI, H. MINAKUCHI and H. HAYASHI. Bulk ammonothermal GaN. *Journal of Crystal Growth* **311**, 10 (2009), 3015–3018.

[59] R. Dwiliński, R. Doradziński, J. Garczyński, L. Sierzputowski, R. Kucharski, M. Zając, M. Rudziński, R. Kudrawiec, J. Serafińczuk and W. Strupiński. Recent achievements in AMMONO-bulk method. *Journal of Crystal Growth* **312**, 18 (2010), 2499–2502.

[60] T. Hashimoto, E. Letts, M. Ikari and Y. Nojima. Improvement of crystal quality in ammonothermal growth of bulk GaN. *Journal of Crystal Growth* **312**, (2010), 2503–2506.

[61] W. C. Röntgen. On a New Kind of Rays. *Nature* **53**, (1896), 274–276.

[62] P. F. Fewster. *X-ray Scattering from Semiconductors*. 2nd ed. London: Imperial College Press, 2003.

[63] W. H. Bragg and W. L. Bragg. The Reflection of X-rays by Crystals. *Proceedings of the Royal Society A: Mathematical, Physical and Engineering Sciences* **88**, 605 (1913), 428–438.

[64] W. Bartels. Characterization of thin layers on perfect crystals with a multipurpose high resolution x-ray diffractometer. *Journal of Vacuum Science & Technology B* **1**, 2 (1983), 338–345.

[65] M. Moram and M. Vickers. X-ray diffraction of III-nitrides. *Reports on Progress in Physics* **72**, (2009), 1–40.

[66] V. Darakchieva, B. Monemar and A. Usui. On the lattice parameters of GaN. *Applied Physics Letters* **91**, 3 (2007), 031911.

[67] V. Darakchieva, T. Paskova, P. P. Paskov, B. Monemar, N. Ashkenov and M. Schubert. Structural characteristics and lattice parameters of hydride vapor phase epitaxial GaN free-standing quasisubstrates. *Journal of Applied Physics* **97**, 1 (2005), 013517.

[68] S. Strite and H. Morkoç. GaN, AlN, and InN: a review. *Journal of Vacuum Science & Technology B* **10**, (1992), 1237–1266.

[69] A. Wright and J. Nelson. Consistent structural properties for AlN, GaN, and InN. *Physical Review B* **51**, 12 (1995), 21–24.

[70] D. Gogova, P. P. Petrov, M. Buegler, M. R. Wagner, C. Nenstiel, G. Callsen, M. Schmidbauer, R. Kucharski, M. Zajac, R. Dwilinski, M. R. Phillips, A. Hoffmann and R. Fornari. Structural and optical investigation of non-polar (1-100) GaN grown by the ammonothermal method. *Journal of Applied Physics* **113**, 20 (2013), 203513.

[71] S. SZE and K. NG. *Physics of semiconductor devices*. New Jersey: John Wiley & Sons, Inc., 2006.

[72] P. P. EWALD. Introduction to the dynamical theory of X-ray diffraction. *Acta Crystallographica Section A* **25**, 1 (1969), 103–108.

[73] E. E. KOCH. *Handbook on synchrotron radiation*. New York: North Holland Publishing Company, 1983.

[74] A. DANILEWSKY, R. SIMON, A. FAULER, M. FIEDERLE and K. BENZ. White beam X-ray topography at the synchrotron light source ANKA, Research Centre Karlsruhe. *Nuclear Instruments and Methods in Physics Research Section B: Beam Interactions with Materials and Atoms* **199**, (2003), 71–74.

[75] R. SIMON and A. DANILEWSKY. The experimental station for white beam X-ray topography at the synchrotron light source ANKA, Karlsruhe. *Methods in Physics Research Section B: Beam* **199**, (2003), 550–553.

[76] L. V. AZÁROFF. *X-ray spectroscopy*. 2nd ed. New York: McGraw-Hill Inc., 1974.

[77] E. HUTTEL, A.-S. MÜLLER, I. BIRKEL and P. WESOLOWSKI. *ANKA Instrumentation Book 2012*. Report. Angströmquelle Karlsruhe ANKA, 2012. (Visited on 22/07/2014).

[78] R. GEHRKE, H. GRAAFSMA, L. INCOCCIA-HERMES, W. LAASCH, T. LAARMANN, W. MORGENROTH, R. RÖHLSBERGER, R. TREUSCH, U. VAINIO and M. V. ZIMMERMANN. *Photon Science 2011*. Hasylab Annual Report. Deutsches Elektronen-Synchrotron Desy, 2011. (Visited on 22/07/2014).

[79] K. WILLE. Synchrotron radiation sources. *Reports on Progress in Physics* **54**, 8 (1991), 1005.

[80] A. VAN STEENBERGEN. Synchrotron radiation sources. *Nuclear Science, IEEE Transactions on* **26**, 3 (1979), 3785–3790.

[81] G. MARGARITONDO. A primer in synchrotron radiation: Everything you wanted to know about SEX (Synchrotron Emission of X-rays) but were afraid to ask. *Journal of Synchrotron Radiation* **2**, 3 (1995), 148–154.

[82] S. L. HULBERT and G. WILLIAMS. *Synchrotron sources*. Report. National Synchrotron Light Source Brookhaven National Laboratory, 1998. (Visited on 27/07/2014).

[83] S. MOBILIO and A. BALERNA. “Introduction to the main properties of Synchrotron Radiation”. Vol. 82.

[84] B. TANNER. *X-ray diffraction topography*. Oxford: Pergamon Press, 1976.

[85] A. LANKINEN. “Synchrotron X-Ray Diffraction Topography of Semiconductor Heterostructures”. Ph.D. Aalto University, 2012. (Visited on 22/07/2014).

[86] W. BERG. Über eine röntgenographische Methode zur Untersuchung von Gitterstörungen an Kristallen. German. *Naturwissenschaften* **19**, 19 (1931), 391–396.

[87] G. RAMACHANDRAN. “X-ray topographs of diamond”. *Proceedings of the Indian Academy of Sciences, Section A*. Vol. 19. 5. Indian Academy of Sciences. 1944, 280–292.

[88] A. GUINIER and J. TENNEVIN. Sur deux variantes de la méthode de Laue et leurs applications. *Acta Crystallographica* **2**, 3 (1949), 133–138.

[89] T. TUOMI, K. NAUKKARINEN and P. RABE. Use of synchrotron radiation in X-ray diffraction topography. *Physica Status Solidi (a)* **25**, 1 (1974), 93–106.

[90] B. RAGHOTHAMACHAR, M. DUDLEY and G. DHANARA. *Handbook of Crystals: X-ray Topography Techniques for Defect Characterization of Crystals*. Berlin: Springer, 2010, 1425–1451.

[91] T. O. TUOMI. Synchrotron X-ray topography of electronic materials. *Journal of Synchrotron. Radiation* **9**, (2002), 174–178.

[92] M. MOORE. White-beam X-ray topography. *Crystallography Reviews* **18**, 3 (2012), 207–235.

[93] B. HENKE, E. GULLIKSON and J. DAVIS. X-ray interactions: photoabsorption, scattering, transmission, and reflection at E=50-30000 eV, Z=1-92. *Atomic Data and Nuclear Data Tables* **54**, 2 (1993), 181–342.

[94] X. HUANG. LauePt, a graphical-user-interface program for simulating and analyzing white-beam X-ray diffraction Laue patterns. *Journal of Applied Crystallography* **43**, (2010), 926–928.

[95] J. LAUGIER and B. BOCHU. *Orient Express v 3.3, a single crystal indexing software*. 2001. URL: http://www.ccp14.ac.uk/tutorial/lmgp/orientexpress.htm (visited on 08/07/2014).

[96] D. K. BOWEN and B. K. TANNER. *High resolution X-ray diffractometry and topography*. CRC Press, 2005.

[97] F. C. FRANK. The influence of dislocations on crystal growth. *Discussions of the Faraday Society* **5**, (1949), 48–54.

[98] B. RAGHOTHAMACHAR, G. DHANARAJ, J. BAI and M. DUDLEY. Defect analysis in crystals using X-ray topography. *Microscopy research and technique* **69**, 5 (2006), 343–58.

[99] J. E. WHITE. X-Ray Diffraction by Elastically Deformed Crystals. *Journal of Applied Physics* **21**, 9 (1950), 855–859.

[100] A. LANKINEN, T. TUOMI, M. KARILAHTI, Z. ZYTKIEWICZ, J. DOMAGALA, P. MCNALLY, Y.-T. SUN, F. OLSSON and S. LOURDUDOSS. Crystal defects and strain of epitaxial InP layers laterally overgrown on Si. *Crystal growth & design* **6**, 5 (2006), 1096–1100.

[101] A. LANKINEN, L. KNUUTTILA, T. TUOMI, P. KOSTAMO, A. SÄYNÄTJOKI, J. RIIKONEN, H. LIPSANEN, P. MCNALLY, X. LU, H. SIPILÄ, S. VAIJÄRVI and D. LUMB. Synchrotron X-ray topography study of defects in epitaxial GaAs on high-quality Ge. *Nuclear Instruments and Methods in Physics Research Section A: Accelerators, Spectrometers, Detectors and Associated Equipment* **563**, 1 (2006), 62–65.

[102] A. LANKINEN, T. LANG, S. SUIHKONEN, O. SVENSK, A. SÄYNÄTJOKI, T. TUOMI, P. MCNALLY, M. ODNOBLYUDOV, V. BOUGROV, A. DANILEWSKY, P. BERGMAN and R. SIMON. Dislocations at the interface between sapphire and GaN. *Journal of Materials Science: Materials in Electronics* **19**, 2 (2008), 143–148.

[103] D. R. BLACK and G. G. LONG. *X-ray Topography*. Special publication 960-10. National Institute of Standard and Technology, 2004.

[104] X. R. HUANG, M. DUDLEY, W. M. VETTER, W. HUANG, W. SI and C. H. CARTER JR. Superscrew dislocation contrast on synchrotron white-beam topographs: an accurate description of the direct dislocation image. *Journal of Applied Crystallography* **32**, (1999), 516–524.

[105] X. R. HUANG, M. DUDLEY, W. M. VETTER, W. HUANG, S. WANG and C. H. CARTER JR. Direct evidence of micropipe-related pure

superscrew dislocations in SiC. *Applied Physics Letter* **74**, 3 (1999), 353–355.

[106] M. DUDLEY, X. HUANG and W. VETTER. Contribution of x-ray topography and high-resolution diffraction to the study of defects in SiC. *Journal of Physics D: Applied Physics* **36**, (2003).

[107] D. B. WILLIAMS and C. B. CARTER. *The Transmission Electron Microscope*. Springer, 1996.

[108] Y. CHEN. "Defects structures in silicon carbide bulk crystals, epilayers and devices". PhD thesis. Stony Brook University, May 2008.

[109] D. ZHUANG and J. EDGAR. Wet etching of GaN, AlN, and SiC: a review. *Materials Science and Engineering: R: Reports* **48**, 1 (2005), 1–46.

[110] P. VISCONTI, K. JONES, M. A. RESHCHIKOV, R. CINGOLANI and H. MORKOÇ. Dislocation density in GaN determined by photoelectrochemical and hot-wet etching. *Applied Physics Letters* **77**, 22 (2000), 3532–3534.

[111] J. WEYHER, P. BROWN and J. ROUVIERE. Recent advances in defect-selective etching of GaN. *Journal of crystal Growth* **210**, (2000), 151–156.

[112] J. WEYHER. Characterization of wide-band-gap semiconductors (GaN, SiC) by defect-selective etching and complementary methods. *Superlattices and Microstructures* **40**, 4-6 (2006), 279–288.

[113] T. HINO, S. TOMIYA, T. MIYAJIMA, K. YANASHIMA, S. HASHIMOTO and M. IKEDA. Characterization of threading dislocations in GaN epitaxial layers. *Applied Physics Letters* **76**, 23 (2000), 3421.

[114] L. LU, Z. Y. GAO, B. SHEN, F. J. XU, S. HUANG, Z. L. MIAO, Y. HAO, Z. J. YANG, G. Y. ZHANG, X. P. ZHANG, J. XU and D. P. YU. Microstructure and origin of dislocation etch pits in GaN epilayers grown by metal organic chemical vapor deposition. *Journal of Applied Physics* **104**, 12 (2008), 123525.

[115] J. WEYHER, S. LAZAR, L. MACHT, Z. LILIENTAL-WEBER, R. MOLNAR, S. MÜLLER, V. SIVEL, G. NOWAK and I. GRZEGORY. Orthodox etching of HVPE-grown GaN. *Journal of Crystal Growth* **305**, 2 (2007), 384–392.

[116] H. MORKOÇ. *Handbook of Nitride Semiconductor Devices. Materials Properties, Physics and Growth*. Vol. 1. Weinheim: Wiley-VCH, 2008, 823.

[117] S. MATHIS, A. ROMANOV, L. CHEN, G. BELTZ, W. POMPE and J. SPECK. Modeling of threading dislocation reduction in growing GaN layers. *Journal of Crystal Growth* **231**, 3 (2001), 371–390.

[118] H. MORKOÇ. *Handbook of Nitride Semiconductors and Devices, Materials Properties, Physics and Growth*. Vol. 1. John Wiley & Sons, 2009.

[119] E. C. YOUNG, F. WU, A. E. ROMANOV, A. TYAGI, C. S. GALLINAT, S. P. DENBAARS, S. NAKAMURA and J. S. SPECK. Lattice Tilt and Misfit Dislocations in (11$\bar{2}$2) Semipolar GaN Heteroepitaxy. *Applied Physics Express* **3**, 1 (2010), 011004.

[120] R. LIU, J. MEI, S. SRINIVASAN, F. A. PONCE, H. OMIYA, Y. NARUKAWA and T. MUKAI. Generation of misfit dislocations by basal-plane slip in InGaN/GaN heterostructures. *Applied Physics Letters* **89**, 20 (2006), 201911.

[121] A. TYAGI, F. WU, E. C. YOUNG, A. CHAKRABORTY, H. OHTA, R. BHAT, K. FUJITO, S. P. DENBAARS, S. NAKAMURA and J. S. SPECK. Partial strain relaxation via misfit dislocation generation at heterointerfaces in (Al,In)GaN epitaxial layers grown on semipolar (1122) GaN free standing substrates. *Applied Physics Letters* **95**, 25 (2009), 251905.

Aalto-DD 187/2014

ISBN 978-952-60-5969-3 (printed)
ISBN 978-952-60-5970-9 (pdf)
ISSN-L 1799-4934
ISSN 1799-4934 (printed)
ISSN 1799-4942 (pdf)

Aalto University
School of Electrical Engineering
Department of Micro- and Nanosciences
www.aalto.fi

BUSINESS +
ECONOMY

ART +
DESIGN +
ARCHITECTURE

SCIENCE +
TECHNOLOGY

CROSSOVER

**DOCTORAL
DISSERTATIONS**